Journal Pre-proof

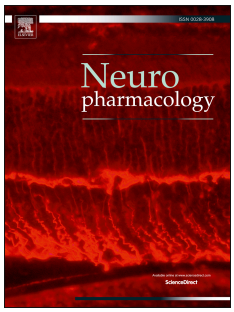

Electrocorticographic, Astrocytic and Transcriptomic Signatures in the Triple Transgenic Mouse Model of Alzheimer's Disease submitted to Stearoyl-CoA Desaturase Inhibition

Audrey Hector, Tanya Leduc, Maria João da Costa Caiado, Benoît Delignat-Lavaud, Julien Dufort-Gervais, Caroline Daneault, Christine Des Rosiers, Clément Bourguignon, Jean-Marc Lina, Karl Fernandes, Jonathan Brouillette, Valérie Mongrain

PII: S0028-3908(26)00008-0

DOI: https://doi.org/10.1016/j.neuropharm.2026.110835

Reference: NP 110835

To appear in: *Neuropharmacology*

Received Date: 22 October 2025

Revised Date: 18 December 2025

Accepted Date: 9 January 2026

Please cite this article as: Hector, A., Leduc, T., Caiado, M.J.d.C., Delignat-Lavaud, B., Dufort-Gervais, J., Daneault, C., Des Rosiers, C., Bourguignon, C., Lina, J.-M., Fernandes, K., Brouillette, J., Mongrain, V., Electrocorticographic, Astrocytic and Transcriptomic Signatures in the Triple Transgenic Mouse Model of Alzheimer's Disease submitted to Stearoyl-CoA Desaturase Inhibition, *Neuropharmacology*, https://doi.org/10.1016/j.neuropharm.2026.110835.

Electrocorticographic, Astrocytic and Transcriptomic Signatures in the Triple Transgenic Mouse Model of Alzheimer's Disease submitted to Stearoyl-CoA Desaturase Inhibition

Audrey Hector,[a-c] Tanya Leduc,[b,c,d,+] Maria João da Costa Caiado,[b,e,+]
Benoît Delignat-Lavaud,[b] Julien Dufort-Gervais,[c] Caroline Daneault,[f] Christine Des Rosiers,[f,g]
Clément Bourguignon,[b] Jean-Marc Lina,[c,h]
Karl Fernandes,[i] Jonathan Brouillette,[a,c] Valérie Mongrain[b,c,d,*]

[a]Department of Pharmacology and Physiology, Faculty of Medicine, Université de Montréal, C.P. 6128, Succ. Centre-Ville, Montreal, QC, H3C 3J7, Canada
[b]Centre de recherche du Centre hospitalier de l'Université de Montréal (CRCHUM), 900 rue St-Denis, Montreal, QC, H2X 0A9, Canada
[c]Center for Advanced Research in Sleep Medicine, Centre intégré universitaire en santé et services sociaux du Nord-de-l'Île-de-Montréal (CIUSSS-NIM), 5400 Gouin West blvd., Montreal, QC, H4J 1C5, Canada
[d]Departement of Neuroscience, Faculty of Medicine, Université de Montréal, C.P. 6128, Succ. Centre-Ville, Montreal, QC, H3C 3J7, Canada
[e]Groningen Institute for Evolutionary Life Sciences, University of Groningen, PO Box 72, 9700 AB Groningen, The Netherlands
[f]Metabolomic platform, Montreal Heart Institute Research Center, 500 Bélanger Street, Montréal, QC, H1T 1C8, Canada
[g]Department of Nutrition, Université de Montréal, Montreal, QC, H3C 3J7, Canada
[h]Département de génie électrique, École de Technologie Supérieure, 1120 Notre-Dame St West, Montreal, QC, H3C 0J8, Canada
[i]Faculty of Medicine and of Health Science, Université de Sherbrooke, 3001, 12e avenue Nord, Sherbrooke, QC, J1H 5N4, Canada
[+]These authors contributed equally to the work.
[*]Corresponding author: valerie.mongrain@umontreal.ca; CRCHUM, 900 rue St-Denis, Montreal, QC, H2X 0A9, Canada

Revised manuscript submitted for publication in: *Neuropharmacology*
Number of figures: 7
Number of supplementary figures: 11
Number of supplementary tables: 10

ABBREVIATIONS: 3xTg: triple transgenic; aCSF: artificial cerebrospinal fluid; AD: Alzheimer's disease; ALDH1L1: aldehyde dehydrogenase 1 family member L1 or 10-formyltetrahydrofolate dehydrogenase; ANOVA: analysis of variance; DAPI: 4′,6-diamidino-2-phenylindole; DAVID: Database for Annotation, Visualization and Integrated Discovery; DEG: differentially expressed gene; DG: dentate gyrus; DMSO: dimethylsulfoxide; ECoG: electrocorticographic; EMG: electromyographic; FC: fold change; GFAP: glial fibrillary acidic protein; IHC: immunohistochemistry; KEGG: Kyoto Encyclopedia of Genes and Genomes; LD: lipid droplet; LH: lateral hypothalamus; MUFA: monounsaturated fatty acid; PBS: phosphate-buffered saline; PS: paradoxical sleep; ROI: region of interest; SCD: stearoyl-CoA desaturase; SCDi: stearoyl-CoA desaturase inhibitor; SEM: standard error of the mean; SFA: saturated fatty acid; SWA: slow wave activity; SWS: slow wave sleep; WT: wild-type.

ABSTRACT

Alzheimer's disease (AD) is associated with cognitive deficits and sleep disturbances. Research suggests the involvement of dysfunctions in lipid metabolism in the brain of AD patients and animal models. The inhibition of stearoyl-CoA desaturase (SCD), a lipid-converting enzyme, was shown to restore memory in triple transgenic (3xTg)-AD mice. In the brain, astrocytes regulate the synthesis of specific lipids. This project tested whether the inhibition of SCD restores sleep in 3xTg-AD mice, and whether this associates with modifications in lipids, astrocytic function and the transcriptome. Wild-type (WT) and 3xTg-AD female mice received a SCD inhibitor (SCDi) or vehicle, which was followed by an electrocorticographic (ECoG) recording. Brain slices were stained for lipid droplets, astrocytic markers or processed for spatial transcriptomics. The reduced time spent awake (increased time spent in slow wave sleep) in 3xTg-AD mice was not restored by SCDi treatment. Rhythmic and scale-free ECoG activities were markedly altered in 3xTg-AD mice for all wake/sleep states, and SCDi changed these ECoG signatures differently in mutant in comparison to WT mice. GFAP-positive cell density and lipid droplet count were elevated in hippocampal CA1, and rescued by SCDi. The treatment also rescued the expression of several genes in a manner mainly overlapping between brain regions. The findings suggest that the multiple wake/sleep alterations in 3xTg-AD mice are not mitigated by SCD inhibition, but that this treatment can revert changes in hippocampal astrocytes, lipids and in the brain transcriptome. This work will benefit the understanding of the AD pathophysiology and associated sleep disturbances.

KEYWORDS: 3xTg-AD mice, lipid-related treatment, slow wave sleep, spectral analysis of the electrocorticogram, scale-free activity, astrocytes, GFAP, ALDH1L1, spatial transcriptomics

INTRODUCTION

Alzheimer's disease (AD), the most common type of dementia, is characterized by a cognitive decline affecting memory and by sleep disturbances (Wang and Holtzman, 2020; Zhang et al., 2022). In fact, sleep disturbances, such as insomnia and fragmented sleep, are proposed to be a major risk factor for the development of cognitive deficits and AD (Shi et al., 2018; Wang and Holtzman, 2020). Multiple alterations in sleep architecture and/or electrocorticographic (ECoG) activity during sleep are also reported in animal models of AD (Dufort-Gervais et al., 2019; Kent et al., 2019; Kosel et al., 2020; Wang and Holtzman, 2020; Hector et al., 2023), including in the widely used triple transgenic (3xTg)-AD mouse model (Benthem et al., 2020; Saber et al., 2021). For instance, 3xTg-AD mice show a reduced number of very long sleep bouts and more sleep during the dark/active period (Saber et al., 2021), together with modifications in the 24-hour rhythm of wheel-running activity (Sterniczuk et al., 2010; Adler et al., 2019).

Patients with AD, together with animal models, were also reported to have alterations in lipids and their metabolism (Chan et al., 2012; Whiley et al., 2014; Hamilton et al., 2015; Chatterjee et al., 2016). Indeed, specific phospholipids were found to be increased in different brain regions and decreased in the plasma of AD patients (Chan et al., 2012; Whiley et al., 2014), and an elevated level of monounsaturated fatty acids (MUFAs) was reported in the AD brain (Fraser et al., 2010; Astarita et al., 2011). In addition, patients suffering from AD were shown to have a higher mRNA expression of stearoyl-CoA desaturase (SCD), the rate-limiting enzyme in the biosynthesis of MUFAs (Astarita et al., 2011). Interestingly, inhibiting SCD was shown to improve different AD-related phenotypes in the 3xTg-AD mouse model, such as the elevated MUFA level and the deficit in spatial memory (Hamilton et al., 2015, 2022). The potential for this intervention to also improve wake/sleep alterations remains to be unveiled.

Alterations in glial functions and neuroinflammation are expected to contribute to the pathophysiology of AD (Heneka et al., 2015). On the one hand, modifications in the well-recognized astrocytic marker glial fibrillary acidic protein (GFAP) have been reported for several brain regions in 3xTg-AD mice (Yeh et al., 2011; González-Molina et al., 2021). Astrocytes play a crucial role in lipid synthesis, distribution, and storage (Lee et al., 2021; Smolič et al., 2021), express SCD (Batiuk et al., 2020; Bedoya-Guzmán et al., 2023), and dysregulation of lipid metabolism in astrocytes can contribute to brain diseases and neurodegeneration (Chen et al., 2023; Mi et al., 2023). Astrocytes have also been implicated in the regulation of ECoG activity during different sleep states (Halassa et al. 2009; Foley et al., 2017), and a higher expression of activated astrocyte marker genes in the prefrontal cortex was reported to be associated with indications of sleep disturbances and cognitive decline in humans (Wu et

al., 2023). Moreover, optogenetic activation of astrocytes was recently shown to rescue sleep oscillations and fear memory in a mouse model of AD (Lee et al., 2023). Therefore, a lipid metabolism-targeting pharmacological intervention for AD could impact sleep via an effect on astrocytic function in key brain regions. On the other hand, genome-wide gene expression studies in AD mouse models, including in 3xTg-AD mice, reveal inflammation and immune response among the top functions affected in different brain regions (Jiang et al., 2023; Widjaya et al., 2023; Barber et al., 2024). Furthermore, targeting lipid metabolism using an inhibition of SCD was shown to restore transcriptomic changes related to the immune system (Hamilton et al., 2022). Interrogating the transcriptome can also help to identify cellular/molecular pathways contributing to modifications in sleep phenotypes under targeted treatments (Ballester Roig et al., 2023).

We here aimed to test the hypothesis that the inhibition of SCD can rescue wake/sleep alterations in 3xTg-AD female mice via a mechanism involving lipids, astrocytes and restoration of the transcriptome in different brain regions. Female mice were focused on in the current study given that AD is more prevalent in women, who generally present a more severe symptomatology (Cao et al., 2020; Gustavsson et al., 2023). In addition, spatial memory was found to be ameliorated by the inhibition of SCD specifically in female 3xTg-AD mice (Hamilton et al., 2022). To test the hypothesis, we used an extensive wake/sleep phenotyping comprising advanced ECoG signal analyses to interrogate variables related to the architecture of vigilance states (i.e., time spent in wakefulness, slow wave sleep [SWS], and paradoxical sleep [PS]; alternations between these states), and to the quality of the ECoG signal during these states. More precisely, standard spectral analyses of the ECoG (e.g., dynamics of slow-wave activity [SWA] during SWS) were combined to an analysis of scale-free activity to quantify rhythmic and arrhythmic ECoG properties, which are both highly relevant to AD (Averna et al., 2023; Wang and Holtzman, 2020). This was done together with quantifications of lipids, an evaluation of astrocytes using measurements of GFAP and aldehyde dehydrogenase 1 family member L1 (ALDH1L1; also known as 10-formyltetrahydrofolate dehydrogenase) in hippocampal regions, the lateral hypothalamus (LH), and thalamic nuclei, and a spatial transcriptomic approach. A treatment of at least 28 days was used to align with the previous literature showing positive effects of this duration of SCD inhibition on neurogenesis and memory in 3xTg-AD female mice (Hamilton et al., 2015, 2022). Our findings reveal that widespread changes in ECoG signatures of the 3xTg mouse model are not ameliorated by SCD inhibition, but that lipidic and astrocytic alterations in the hippocampus as well as genome-wide gene expression changes in several brain regions can be restored (at least in part) by inhibiting SCD. This research increases the knowledge about the complex relationship between sleep, lipids and glial cell in the context of neurodegeneration.

MATERIAL AND METHODS

Animals and protocol

Four-month-old female 3xTg-AD mice (B6;129-Tg(APPSwe,tauP301L)1Lfa *Psen1*^{tm1Mpm}/Mmjax, Jackson Laboratory MMRRC strain #034830-JAX) and WT mice (B6129SF2/J, Jackson Laboratory strain #101045) were used in this study. The 3xTg-AD mouse model features three mutations associated with familial AD, namely APP Swedish, MAPT P301L, and PSEN1 M146V (Oddo et al., 2003). It presents an age-dependent progressive AD-like neurodegeneration, including amyloid β deposition in different brain areas and synaptic dysfunctions (Belfiore et al., 2019; Oddo et al., 2003). Importantly, 3xTg-AD females show worse phenotypes than males regarding amyloid β pathology (Hirata-Fukae et al., 2008), which is in line with the higher risk of developing AD in women, the higher worldwide prevalence of AD in women, and the generally higher severity of the disease in women (Cao et al., 2020; Gustavsson et al., 2023; Lautenschlager et al., 1996). The targeted age for the beginning of treatment (i.e., four months) was guided by findings in this mouse model of elevated lipid droplets (LDs) at two months of age (Hamilton et al., 2015), elevated intraneural amyloid β in the hippocampus and cerebral cortex and memory retention deficits at four months (Billings et al., 2005), and reduced synaptic protein level at four months in females (Dufort-Gervais et al., 2020). An early intervention was favored to act before extensive neuronal damage occurs. Mice were maintained at the CRCHUM, and sent to the Hôpital du Sacré-Cœur de Montréal (CIUSSS-NIM) for experiments where they were individually housed under a 12-hour light/12-hour dark cycle at 23-25 °C room temperature with free access to food and water for the full duration of the experiment.

Mice of each genotype were assigned to one of two treatment groups, namely treatment with SCD inhibitor (SCDi) or with vehicle, for a total of four experimental groups: WT mice with vehicle (n = 12; age and weight at the time of surgery ± standard error of the mean: 19.3 ± 0.3 weeks, 20.5 ± 0.5 g), WT with SCDi (n = 12; 18.8 ± 0.3 weeks, 21.5 ± 0.7 g), 3xTg mice with vehicle (n = 11; 19.1 ± 0.3 weeks, 25.2 ± 1.1 g), and 3xTg with SCDi (n = 10; 19.0 ± 0.2 weeks, 25.8 ± 1.2 g). Mice were implanted with osmotic minipump for treatment infusion and with electrodes for ECoG and electromyography (EMG) during the same surgical procedure (described below; Fig. S1A). At 28 days of treatment (theoretical infusion duration, see below), ECoG/EMG signals were recorded for 24 hours starting at light onset (= Zeitgeber time 0: ZT0). Two days after the end of ECoG/EMG recordings, animals were sacrificed by cervical dislocation between ZT2 and ZT6 (Fig. S1A), and brains were immediately sampled, separated into left and right hemispheres along the middle sagittal line, and frozen on dry ice. This design was applied to measure lipids, astrocytic markers and the transcriptome in animals with ECoG/EMG

recording with a minimal time interval between measurements, which prevented an additional recording period (e.g., after the end of treatment). All procedures with animals were conducted according to the guidelines of the Canadian Council on Animal Care, and the protocol was approved by the *Comité d'éthique de l'expérimentation animale* of the CIUSSS-NIM. In addition, all analyses were carried out by experimenters who were blind to animals' group. A preprint article reporting some of the wake/sleep and astrocyte findings was previously published (Hector et al., 2024).

Surgical procedures and ECoG recording

Similar to conducted previously (Hamilton et al., 2015, 2022), osmotic minipumps (Alzet® model 1004; 0.11 µl/hour infusion rate) were filled 48 hours prior to surgical implantation with the SCDi (Abcam #ab142089) dissolved in dimethylsulfoxide (DMSO; Sigma-Aldrich) and diluted in sterile artificial cerebrospinal fluid (aCSF; Harvard Apparatus # 59-7316) for a final infusion concentration of 80 µM. The inhibitor ($C_{20}H_{22}ClN_3O_3$) was chosen for its selectivity for SCD and potency (IC_{50} = 4.5 nM), for its good tolerability when administered intracerebroventricularly, and especially for its effects on MUFAs and spatial memory (Hamilton et al., 2015, 2022). Control/vehicle pumps were filled with the same volume (i.e., 100 µL) of 0.8% DMSO/aCSF. For this volume, the nominal (theoretical) duration of infusion is 28 days but the actual duration is closer to 36 days (which includes the two days pre-implantation). Osmotic pumps were assembled to a cannula (Plastics One #3280P) via PE tubing immediately after filling. For implantation, mice were deeply anesthetized with ketamine/xylazine (120/10 mg/kg, intraperitoneal injection) combined to continuous isoflurane (0.5-2%, inhalation), and were installed in a stereotaxic frame. Mice were implanted with ECoG and EMG electrodes similar to previously described (El Helou et al., 2013; Areal et al., 2020; Ballester Roig et al., 2023). ECoG electrodes (J.I. Morris Inc. screws #FF00CE125) targeted the motor cortex (1.5 mm anterior to the bregma, 1.5 mm lateral right to the midline) and the visual cortex (1.0 mm anterior to the lambda, 1.5 mm right to the midline), a reference electrode was located above the somatosensory cortex (0.7 mm posterior to the bregma, 2.6 mm right to the midline; Fig. S1A), and EMG electrodes (Delta Scientific 99.99% gold wire 0.2 mm diameter annealed) were implanted in neck muscles. During the same surgery, mice were implanted with the osmotic pump under the skin of their back, and with the cannula for intracerebroventricular targeting with the following coordinates: 0.8 mm posterior to the bregma, 2.3 mm left to the midline, and 2.05 mm below the skull surface with a 27.5º angle left from the vertical plane to avoid interference with ECoG/EMG electrodes. The cannula and electrodes were then fixed to the skull using dental cement (3M RelyX Unicem 2 automix), and electrodes were soldered to a 6-channel connector (ENA AG #BPHF2-O6S-E-3.2). Implanted mice were monitored two times per day for the first three days post-surgery. Five days before the end of the 28-day (nominal) treatment, mice were habituated

to cabling conditions for five consecutive days, which was immediately followed (no cabling interruption) by a recording of ECoG/EMG signals lasting 24 consecutive hours and conducted under undisturbed conditions at 256 Hz using the Stellate Harmonie software (Natus) and Lamont amplifiers.

ECoG analyses

Vigilance states (i.e., wakefulness, SWS, PS) were visually assigned to 4-second epochs using bipolar ECoG (motor - visual cortex) and EMG signals as previously described (Ballester Roig et al., 2023; Hector et al., 2023). Artifacts were simultaneously identified and excluded from spectral and scale-free ECoG analyses. The time spent in each vigilance state was averaged for the full 24-hour recording, for the 12-hour light and dark periods, as well as per hour. The number of bouts of different durations was computed for the full 24-hour recording separately for each vigilance state. The bipolar and unipolar (motor and visual cortex separately) ECoG signals were submitted to spectral analysis using a Fast Fourier transform (mean suppression, extended cosine bell, 4-sec window, 4-sec interval [no overlap]) to compute spectral power between 0.5 and 50 Hz with a 0.25 Hz resolution for the full 24-hour recording and/or per 12-hour light and dark periods for each state. Power spectra were expressed as a percent of the mean power of all 0.25-Hz bins of all states for each mouse to interrogate the relative contribution of all frequencies (i.e., relative power spectra). Absolute and relative activity for the full 24-hour recording and 12-hour periods were also calculated for six different frequency bands (i.e., SWA 0.5-5 Hz, Theta 5-9 Hz, Alpha 9-12 Hz, Sigma 12-16 Hz, Beta 16-30 Hz, Gamma 30-50 Hz). In addition, the 24-hour time course of SWA and Theta activity during wakefulness and SWS was calculated using averages per time intervals to which an equal number of epochs contributed and expressed relative to the 24-hour mean activity for each band and each mouse as described previously (Areal et al., 2020; Ballester Roig et al., 2023; Hector et al., 2023).

Parameters related to scale-free ECoG activity were computed using a Wavelet-Leaders formalism similar to previously described (Lina et al., 2019; Areal et al., 2025), which was developed as a function of earlier methodologies (Ciuciu et al., 2008; Wendt et al., 2009). Briefly, a Daubechies wavelet with six vanishing moments was used to evaluate the $1/f^{\gamma}$ power decay of the spectral power as a function of frequency plotted in log-log scales (frequency range 0.5 to 64 Hz) and to compute the Hurst exponent (H) from the scaling exponent γ (indicative of the slope of this spectral power decay; i.e., $\gamma = 2H + 1$). Since the ECoG power spectrum is not monofractal, but rather composed of multiple Hs (Ma et al., 2005; Weiss et al., 2009), the most prevalent Hurst exponent (Hm) and the dispersion (D) of Hs around Hm were extracted using the multifractal Wavelet-Leaders approach. Hm reflects the long-range dependencies of different ECoG time scales with 0.5 generally considered as the value separating persistence (> 0.5) and anti-persistence (< 0.5). It has been calculated for the artifact-free bipolar signal of each vigilance state

for the full 24-hour recording and for the same time intervals as frequency bands described above. The same was done for the multifractal parameter D, with higher absolute D linked to higher complexity (i.e., higher instability and dispersion of Hurst exponents). These two parameters were also computed for the unipolar ECoG signals of each vigilance states for the full 24-hour recording. Two animals had to be excluded from both spectral and scale-free ECoG analyses of the bipolar and visual cortex signals because of predominant artifacts (one WT mouse receiving vehicle and one receiving SCDi). For specific sets of analyses, additional exclusions occurred mainly because of an absence of artifact-free epochs in some intervals (in particular for PS) or of outlier values.

Fatty acid analyses

Left hemispheres (n = 7 per experimental group, except n = 6 for 3xTg mice receiving SCDi) were processed by the Montreal Heart Institute Metabolomic platform for quantitative profiling of 29 fatty acids by gas chromatography-mass spectrometry using previously described methods (Gelinas et al., 2011; Thompson et al., 2015; Turcot et al., 2015). In brief, 50 mg of pulverized brain tissues were incubated overnight at 4 °C in a solution of chloroform/methanol (2:1) containing 0.004 % butylated hydroxytoluene (BHT), filtered through gauze and dried using nitrogen gas. Triglycerides and phospholipids plus free fatty acids were eluted in separated fractions on an aminopropyl column (500 mg Bond Elut LRC-NH2, Agilent Technologies Inc., Santa Clara, CA, USA). Fatty acids were analyzed as their methyl esters after direct transesterification with acetyl chloride/methanol on a 7890B gas chromatograph coupled to a 5977A mass selective detector (Agilent Technologies Inc.) equipped with a capillary column (100 m x 250 μm inner diameter J&W Select FAME CP7420, Agilent Technologies Inc.) and operated in the positive chemical ionization mode using ammonia as reagent gas at the following conditions: injection (0.5-2 μL) at 270 °C in a split mode (ratio 50:1) using high-purity helium as the carrier gas (constant flow rate: 0.44 mL/min) and the following temperature gradient: 190 °C for 25 minutes, increased by 1.5 °C/minute until 236 °C. Fatty acids were analyzed as their [M+NH3]+ ions by selective ion monitoring. Quantification was achieved using standard curves and isotope-labeled internal standards, and expressed as absolute concentration (nmol/mg). Results are presented for triglycerides and phospholipids plus free fatty acids fractions.

Quantification of lipid droplets (LDs)

Right hemispheres (n = 4 per WT group and n = 5 per 3xTg group) were submitted to LD staining using LipiDye II (Dc DiagnoCine #FNK-FDV-0027) similar to previously described (Petrelli et al., 2024). LipiDye II was specifically selected for the capacity to detect LDs, including small LDs, on brain slices prepared from frozen brains, and for the high photostability. It was recently shown to tightly

colocalize with the LD-associated protein perilipin 2 (Petrelli et al., 2024). Three hemisphere sections ranging from 1.22 mm to 2.46 mm posterior to the bregma (covering the dorsal hippocampus) were used for analysis of CA1 and CA3. Sections were fixed with 10 % formalin for 30 minutes at room temperature. After three washes with phosphate-buffered saline (PBS; Sigma-Aldrich #P5368), slices were incubated for two hours at room temperature under agitation and protected from light with 1 µM LipiDye II. Sections then were washed twice in PBS, mounted with Prolong Glass with NucBlue (Invitrogen #P36984), and stored at 4 °C prior to imaging. Two regions of interest (ROIs) were selected for both CA1 and CA3 regions for each of the three slices used per mouse (total of 6 ROIs per region per animal, all *stratum pyramidale* for which LDs were clearly observed). Images were acquired using an Axio Imager M2 Apotome (Zeiss) with a 63X oil immersion objective (Plan-Apochromat 63X/1.4 Oil DIC M27, Zeiss) and X-Cite 120 LED Boost lasers (Excelitas) set at 353 nm (NucBlue) and 488 nm (LipiDye II). Z-stacks were taken at 0.3 µm intervals, and images were corrected for local bleaching, deconvolved using regularized inverse filtering, and background subtracted using the Zen software.

LDs were quantified using the open-source software Ilastik (version 1.4.0.post1). Briefly, a pixel classification pipeline was trained on six representative images to differentiate LD signal from background. The trained model was then applied to the whole dataset to generate predictive maps (Fig. S1B and S1C). A hysteresis thresholding method with object size filtering was then used to refine signal segmentation (minimum 2 pixels and maximum 100,000,000 pixels; Fig. S1C). Further classification was performed to differentiate individual LDs from clusters of LDs, where clusters were defined as aggregated LD signals spanning multiple focal planes (x, y and z axes) that could not be reliably segmented as 3-dimension single objects (Fig. S1C). The total number of individual LDs and LD clusters in each Z-stack was then normalized to the number of cells per field. Cell counting was achieved with ImageJ (v1.54g) by using NucBlue staining Z-projections of each Z-stack, and by applying a median filter (radius = 25) and maxima automatic detection (prominence = 45). Each parameter was optimized through manual validation on a representative subset of six images. Two brains exhibiting a high background noise were manually quantified to ensure accuracy. In CA1 only (not in CA3), cell count was significantly lower in mutant compared to WT mice ($F_{1,102}$ = 8.7, p = 0.004) and significantly higher under SCDi compared to vehicle ($F_{1,102}$ = 9.8, p = 0.002), justifying the need to express LDs as a value per cell. To normalize data distribution, the number of LDs per cell and the number of LD + clusters per cell were log-transformed prior to statistical analysis and graphing.

Immunohistochemistry (IHC)

Twenty-three right hemispheres (n = 6 per experimental group, except n = 5 for 3xTg mice receiving SCDi) were used for IHC to count the number of GFAP- and ALDH1L1-positive cells and

conduct a morphological analysis. The focus was specifically on astrocytic markers for the current study and microglial markers were not used because microglia were previously thoroughly investigated in the hippocampus of the same mouse model exposed to the same treatment (Hamilton et al., 2022). Thirty µm coronal slices of hemispheres were cut at -18 ± 1 °C using a cryostat (Leica #CM3050 S), and slices were directly mounted on Superfrost Plus™ slides (Fisher Scientific #1255015) and stored at -80 °C until processing. For IHC, one slice per animal located between 1.94 mm and 2.18 mm posterior to bregma was used to capture a similar region of the thalamus, LH, and dorsal hippocampus. Slides were first placed at -20 °C for 8 minutes, and then at room temperature for 4 minutes, following which they were fixed for 30 minutes in 10 % formalin (Sigma-Aldrich #R04586-76), and washed 3 times 5 minutes in PBS. Each slide was then dried around the slices, which were isolated using a PAP pen (IHC WORLD #SPM0928). The slides were then incubated for 60 minutes at room temperature in blocking buffer (PBS with 5 % goat serum [Abcam #ab7481] and 0.3 % Triton X-100 [Bio-Rad Laboratories #161-0407]). After removing the blocking buffer and re-applying PAP pen, the slides were incubated overnight at 4 °C with primary antibodies (anti-GFAP 1:1000, Invitrogen #PA1-10004; anti-ALDH1L1 1:1000, Abcam #ab87117) diluted in PBS with 1 % bovine serum albumin (Winset Inc. #800-095-EG) and 0.3 % Triton X-100. After 4 times 5-minute washes in PBS with 0.5 % Tween® 20 (Fisher Scientific #9005-64-5), each slide was again dried around tissue slices and PAP pen was re-applied. The slides were then incubated 90 minutes in the dark at room temperature with the corresponding secondary antibodies (Alexa Fluor 647 1:1000, Abcam #ab150171; Alexa Fluor 555 1:1000, Invitrogen #A-21429) diluted in PBS with 1 % bovine serum albumin and 0.3 % Triton X-100. After additional 5-minute washes with 0.5 % Tween 20 in PBS, ProLong® Gold antifade reagent with 4′,6-diamidino-2-phenylindole (DAPI; Invitrogen #P36931) was added to each slide, which were immediately mounted with a glass coverslip (#1.5 thickness; Epredia™ #152455). The slides were sealed with nail polish, and stored in the dark at 4 °C until imaging.

IHC image acquisition and analyses

All images were acquired using a confocal microscope (Zeiss LSM 900 with Airyscan 2). For cell counting, images were acquired with a 20X lens (plan-Apochromat 20X/0.8 NA M27) and a 2X digital zoom using a Z-stack (average interval between sequential sections of 0.47 µm). Then, non-overlapping ROIs of the same size were captured: four in the CA1 (stratum radiatum), four in the CA3 (stratum radiatum and lucidum), four in the dentate gyrus (DG; stratum moleculare), six in the ventral posterolateral and ventral posteromedial nuclei of the thalamus, and four in the LH for each animal (Fig. S2A to S2C). Image acquisition was done with a pinhole aperture of one airy unit and the following settings: GFAP excitation = 652 nm, emission = 669 nm; ALDH1L1 excitation = 553 nm, emission = 568

nm; DAPI excitation = 358 nm, emission =461 nm; collected in all channels. Cell counting was performed for each region of interest on the maximum intensity Z-projection images using the "Cell Counter" plug-in of Fiji (ImageJ 1.54f), and Z-stacks were used for the validation of the counts. A cell was counted when the specific marker (GFAP or ALDH1L1) co-localized with the nuclear stain DAPI. Given our observation of a low GFAP staining in the thalamus and LH, and of a puncta-like ALDH1L1 staining in hippocampal areas, GFAP-positive cells were counted only for hippocampal areas and ALDH1L1-positive cells only in the thalamus and LH. Cell counts were normalized to the size of the counted regions to be reported as cell densities.

A morphological analysis using a skeletonization pipeline applied to the GFAP staining was adapted from a previously described method (Tavares et al., 2017). For this analysis, images were acquired using the same microscope and a 40X oil immersion lens (plan-Apochromat 40X/1.3 NA oil DIC [UV] VIS-IR M27 with a 2X digital zoom) also with a Z-stack approach (average interval between sequential sections 0.25 µm). A laser power correction was applied through the Z-stack to optimize detail and avoid photobleaching. A total of six astrocytes (non-overlapping regions of size 79.86 x 79.86 µm) per mouse were collected from the CA1 stratum radiatum, and GFAP and DAPI channels were merged. Only astrocytes with clear GFAP-positive processes extending in more than one direction and a DAPI-positive nucleus were considered and skeletonized (Fig. S2D, left panel). The skeletons of the GFAP-positive processes were extracted using the "Simple Neurite Tracer" plug-in of Fiji (Fig. S2D, middle panel), and analyzed using the built-in feature "Measure" to obtain three parameters: radius from the soma (radius in µm from the cell body center to the outermost sphere containing all processes/branches of the astrocyte; see also Sholl analysis below), mean length of processes/branches (µm), and total length of processes/branches (µm). In addition, a Sholl analysis was performed using a sphere radius increment of 4 µm (Fig. S2D, right panel), similar to previously described for astrocytes (Klein et al., 2020; Tavares et al., 2017).

Given the observation of puncta-like ALDH1L1 staining in the CA1 region of the hippocampus, we decided to count the number of ALDH1L1 puncta associated to GFAP-positive astrocytic processes. To do so, the GFAP/DAPI Z-stack was used to define a frame range covering most of the astrocyte, and three frames of the ALDH1L1 Z-stack were randomly chosen within this range (Fig. S2E, left panel). The skeleton of the corresponding astrocyte was then converted into a "mask" using the "Fill out" setting of "Simple Neurite Tracer" at a threshold of 0.005 (threshold enough to cover different branch thicknesses while remaining conservative; arbitrary unit). This mask was then applied to each of the three ALDH1L1 frames to isolate the ALDH1L1 puncta associated with the corresponding astrocyte (Fig. S2E, middle panel). This was done using Gaussian background subtraction with a relative threshold of 0.03 to 0.1 % (Fig. S2E, right panel). ALDH1L1 puncta were then automatically counted,

and counts obtained from the three frames were averaged per astrocyte (n = 6 astrocytes per mouse). This method was validated on small segments of the image for which manual counts were compared to the software-generated counts.

Statistical analyses

Statistical analyses were performed using the software Prism (GraphPad) or Statistica (StatSoft). Two-way analyses of variance (ANOVA) were used with factors Genotype and Treatment to compare wake/sleep variables average per 24-hour recording or 12-hour periods between experimental groups, as well as triglycerides and phospholipids plus free fatty acids, LDs, GFAP- and ALDH1L1-positive cell densities, and GFAP-derived morphological parameters. Three-way repeated-measure ANOVA with factors Genotype, Treatment, and light/dark Period, Hour, Interval or Distance from the soma were used to compare the time course of time spent in vigilance states, of activity in frequency bands, of scale-free parameters, and the Sholl analysis-extracted morphology of astrocytes. Tukey's post hoc tests or planned comparisons were used to decompose significant effects where appropriate, and significance levels of repeated-measure designs were corrected using the Huynh-Feldt correction when needed. Results are presented as mean ± standard error of the mean (SEM), and the threshold for statistical significance was defined as $p < 0.05$. Table S1 features the results of most statistical comparisons. The size of analyzed samples is indicated in the legend of each figure.

Spatial transcriptomics

Four left hemispheres, one per experimental condition described in the section Animals and protocol (i.e., WT receiving vehicle, WT receiving SCDi, 3xTg receiving vehicle, 3xTg receiving SCD), were sliced with a cryostat (Leica #CM3050 S), and 10-µm thick coronal slices positioned approximately at 2.0-2.2 mm posterior to the bregma (covering the cerebral cortex, hippocampus, thalamus, hypothalamus) were processed according to the 10x Genomics Visium Tissue Preparation protocol (CG000240-Rev D). Slices were mounted onto a chilled Visium Spatial Gene Expression slide (10x Genomics), incubated at 37 °C for one minute, and then submerged in methanol for 30 minutes at -20 °C for fixation. Hematoxylin-Eosin staining was then performed according to the 10x Genomics protocol (CG000160-Rev C), and images were acquired with an Olympus Optical microscope (#BX61VSF 241; 10X objective Olympus UPLSAPO10x with 0.4 numerical opening). It should be noted that subtle differences in the exact antero-posterior location of the coronal slices were observed between groups and were carefully considered during analysis.

The 10x Genomics Visium Spatial Gene Expression protocol (CG000239-Rev D) was followed for library preparation similar to previously done (Ballester Roig et al., 2023). Brain slices were

permeabilized at 37 °C for 18 minutes before being covered with a reverse transcription mastermix for 45 minutes at 53 °C. The obtained complementary DNA (cDNA) was incubated with 0.08 M KOH, washed with elution buffer, and then incubated with another mastermix for second strand synthesis at 65 °C for 15 minutes. The remaining tissue was finally denatured, and samples were amplified using a cDNA amplification mix: 98 °C for 3 minutes, 16 cycles of 15 seconds at 98 °C + 20 seconds at 63 °C + one minute at 72 °C, then 72 °C for one minute. SPRIselect beads (Beckman Coulter, Cat# B23318) were used to clean the cDNA, which was then submitted to a cDNA fragmentation, end repair and A-tailing protocol. SPRIselect beads were also used for post-ligation cleanup. Samples were then amplified using an amplification mix with sample indexes i5 and i7 (necessary for P5/P7 Illumina paired-end sequencing): 98 °C for 45 seconds, 19 cycles of 20 seconds at 98 °C + 30 seconds at 67 °C + 20 seconds at 72 °C, then 72 °C for one minute. The cDNA was finally purified with SPRIselect beads, and resulting libraries were stored at -20 °C.

RNA sequencing (RNAseq) was performed with the platform Illumina NovaSeq PE100 by Genome Quebec (Montreal, Canada), at a sequencing depth of approximately 2,500 M read pairs per sample. Briefly, libraries were quantified using the KAPA Library Quantification Complete kit (Kapa Biosystems), and average fragment size was determined using a Fragment Analyzer 5300 instrument (Agilent). The libraries were normalized and pooled, and then denatured in 0.02 N NaOH and neutralized using HT1 buffer. The pool was loaded at 200 pM on a Illumina NovaSeq S4 lane using Xp protocol as per the manufacturer's recommendations. The run was performed for 2 x 100 cycles (paired-end mode, including 10 cycles for each index [i7 and i5]). A phiX library was used as a control and mixed with libraries at 1 % level. Base calling was performed with RTA v3 and the program bcl2fastq2 v2.20 was used to demultiplex samples and generate fastq reads. Then, raw sequencing files (FASTQ) and histology images were processed with the SpaceRanger 2.1.1. software (10x Genomics) and the "spaceranger count" pipeline to align sequencing reads to the mouse reference genome (mm10), to conduct spatial barcode assignment, and to quantify gene expression for each spatial spot. Across the four tissue slices, the total number of reads ranged from 587 to 814 M, the mean number of read per spatial spot ranged from 200,000 to 264,000, and the median unique molecular identifier (UMI) count per spot ranged from 10,000 to 12,000. The percentage of reads mapped to the genome was consistently high, ranging from 94.8 to 96.2 %.

The pipeline "spaceranger aggr" was then used to aggregate and normalize gene expression data across the different experimental conditions. This pipeline was initially run with the four experimental conditions (WT treated with vehicle, WT treated with SCDi, 3xTg treated with vehicle, 3xTg treated with SCDi) to identify spatial spots belonging to common brain regions as defined by gene expression clusters, following which the pipeline was run with pairs of experimental conditions to adjust for

differences in sequencing depth across samples and to perform statistical comparisons. More precisely, differentially expressed genes (DEGs) were computed between 3xTg and WT both treated with vehicle to identify genes affected by genotype, between WT treated with vehicle and SCDi to identify genes changed by SCDi in WT, between 3xTg treated with vehicle and SCDi to identify genes changed by SCDi in mutant mice, and finally between 3xTg and WT both treated with SCDi to identify genes differentially impacted by treatment in the two genotypes. These analyses can be considered exploratory because of the single biological replicate per experimental group. The Loupe Browser v8.0 (10x Genomics) was used to analyze gene-spot matrices with a significance threshold set to a False Discovery Rate [FDR] value < 0.05 (Benjamini-Hochberg correction for multiple comparisons) and to produce spatial maps.

Gene ontology enrichment analyses, including Kyoto Encyclopedia of Genes and Genomes (KEGG) pathway, were performed using the Database for Annotation, Visualization and Integrated Discovery (DAVID) online tool (https://david.ncifcrf.gov/tools.jsp). Given that this tool can only accept 3,000 genes, only the top 3,000 DEGs were used when application (i.e., DEGs with the lowest FDR values comprising DEGs with increases or decreases in expression). Redundant pathways were not included in graphical representations. Lists of DEGs were submitted to clustering using ward.D2 (in R), and R codes were used to produce volcano plots and heatmaps. Spatial maps and violin plots presented are direct outputs of the Loupe Browser.

RESULTS

More time spent in SWS in 3xTg mice is not impacted by SCDi

We first observed that wake/sleep architecture alterations in 3xTg-AD female mice in comparison to WT mice were not significantly impacted by the inhibition of SCD. Mutant mice were found to spend significantly less time awake and more time in SWS than WT mice during the full 24-hour recording (Fig. 1A and Table S1A), which was driven by specific differences during the 12-hour dark period (Fig. 1B and Table S1A). Indeed, the 24-hour distribution of wake/sleep states was significantly modified in 3xTg-AD mice, which spent less time awake in the middle of the dark period, more time in SWS during the same hours, and less time in PS around the light to dark transition (Fig. 1C and Table S1A). SCDi treatment did not significantly impact time spent awake, in SWS and PS, and also did not affect state distribution across 24 hours (Table S1A).

In general, mutant mice showed more individual bouts of wake and SWS states (Fig. 1D and Table S1A), which is indicative of a higher fragmentation (less consolidation) of vigilance states. This

phenotype was also not significantly modified by inhibiting SCD for at least 28 days (although a trend was observed for very short wake bouts [4-second bouts] to be rescued to WT vehicle values in 3xTg treated with SCDi; Table S1A). Independent of genotype, SCDi only increased the number of SWS bouts of 2 minutes (Fig. 1D and Table S1A). These findings reveal major modifications in wake/sleep amount and alternation in 3xTg female mice, including more SWS during the active (dark) period and elevated wake/SWS fragmentation, which are not significantly reverted by a four-week inhibition of SCD.

Lower ECoG absolute power in 3xTg mice and effects of SCDi on relative power

The spectral profile of the ECoG within the different vigilance states, interrogated using a spectral analysis, can be considered an indication of state quality. It was investigated using a standard bipolar (motor - visual) signal for both absolute and relative power because the first informs on, for instance, changes in the organization of the cerebral cortex, whereas the second is indicative of the relative contribution of the different frequency components of the signal. The 24-hour mean absolute power spectra computed between 0.5 and 50 Hz showed significant lower spectral power for a wide range of frequencies for the three vigilance states in 3xTg mice in comparison to WT mice (Fig. 2A). More precisely, when assessing spectral activity in distinct frequency bands, a significant lower power in 3xTg was found for SWA, Theta, Alpha, Sigma and Beta frequency bands measured during both wakefulness and SWS (Fig. S3A and Table S1B). During PS, lower power in mutant mice was significant for Sigma, Beta and Gamma frequency bands (Fig. S3A and Table S1B). The absolute power measured for the six frequency bands was not significantly impacted by SCDi treatment for all three states (Fig. S3A and Table S1B). These observations indicate a global reduction in ECoG spectral power in 3xTg mice that encompasses all vigilance states.

Interestingly, the 24-hour mean relative power spectra revealed significant effects of SCD inhibition for wakefulness and PS that are dependent on genotype (Fig. 2B). More precisely, 3xTg mice treated with SCDi showed a higher relative power than treated WT mice in the Beta and Gamma bands (Fig. S3B and Table S1B). The same observations were made when examining specifically the light period, as well as the Gamma band during wakefulness and the Sigma and Beta bands during PS when considering the dark period (Fig. 2C and Table S1B). These findings suggest that SCDi affects the relative power in faster frequencies during wake and PS in an opposite manner in 3xTg mice in comparison to WT mice; increasing it in the former and decreasing it in the second. Opposite effects of the treatment on ECoG spectral signatures (relative power) of mutant and WT mice were also found when considering separately the signals of the motor and visual cortex, and appeared particularly manifest for the visual cortex (Fig. S4A and S4B).

The 24-hour mean relative power also differed between genotypes in other frequency bands. More precisely, a significant lower relative contribution in 3xTg mice in comparison to WT mice was found for the Theta and Alpha bands during wakefulness and the Sigma band during SWS, whereas the opposite was found for SWS Gamma as well as SWA and Alpha during PS (Fig. S3B and Table S1B). In general, these genotype differences were also significant when assessing relative power separately for the light and dark periods, as well as when considering separately the motor and visual cortex (Fig. 2C, Fig. S4A and S4B, and Table S1B). In sum, mutant mice present major alterations in the relative contribution of different frequency bands during all three vigilance states, alterations that are not normalized to values of WT by the inhibition of SCD.

The changes in SWA during SWS and Theta activity during wakefulness occurring as a function of the nychthemeron are considered an index of the homeostatic process that regulates sleep (Vassalli and Franken, 2017). The 24-hour variations in SWA and Theta activity measured during wakefulness and SWS were thus compared between groups to investigate the impact on the daily dynamics of the activity in these frequency bands (Fig. 2D and 2E, and Table S1B). The dynamics of SWA during SWS and of Theta activity during wake and SWS was significantly impacted by genotype, with higher activity near the middle of the light period and lower activity during the dark period in 3xTg mice in comparison to WT mice, resulting in a generally lower amplitude of daily variations in mutant animals. Similar observations were made for the 24-hour dynamics of SWS SWA computed separately for the motor and visual cortex (Fig. S4C and S4D). SCDi treatment did not significantly impact the daily variations in SWA and Theta activity during wakefulness and SWS for bipolar analyses, but changed wake Theta activity dynamics of the visual cortex (Fig. 2D and 2E, Fig. S4D, and Table S1B). These findings suggest that genotype importantly impacts the 24-hour dynamics of slower ECoG activity, which is only modestly altered by SCDi.

More anti-persistence of the wake/SWS ECoG in 3xTg mice

The scale-free activity of the ECoG informs on signal complexity of the different states by assessing the relationship between activity at all different time scales. As described in methods, Hm (indicative of persistence across scales), and D (dispersion around Hm and degree of multifractality) have been extracted from the bipolar and unipolar signals. For the bipolar signal, the 24-hour mean Hm was significantly lower in 3xTg than in WT mice for wakefulness and SWS, but not for PS (Fig. 3A, first column; Table S1C). The 24-hour variations of Hm was also found to differ between genotypes for wakefulness and SWS, but not for PS (Fig. 3A, second column; Table S1C). More precisely, lower Hm in 3xTg mice in comparison to WT mice appeared more prominent during the dark period for wakefulness, and at the beginning of the light period and end of the dark period for SWS. A lower Hm in 3xTg mice

suggests more anti-persistence (less persistence) across ECoG time scales during wakefulness and SWS, which was also significant when analyzing separately the motor and visual cortex (Fig. 3B and 3C; Table S1C). This suggest that the effect of 3xTg mutations on Hm is state-dependent and relatively global, observable for two distant regions of the cerebral cortex. There was no significant effect of the SCDi treatment on the Hm 24-hour mean or 24-hour variations for all states (Table S1C).

The 24-hour mean D was also found to differ between genotypes in a state-dependent manner: D being significantly more negative (i.e., more multifractal) in 3xTg mice in comparison to WT mice during wakefulness for all analyzed ECoG signals but only for the motor cortex during SWS (Fig. 3D to 3F; Table S1C). The more negative wakefulness D for the bipolar signal in 3xTg mice in comparison to WT mice was independent of time-of-day as indicated by the 24-hour dynamics (Fig. 3D, second column; Table S1C). For wakefulness and SWS, SCDi treatment did not impact D for the three ECoG signals (Table S1C). However, during PS, the 24-hour mean of the bipolar and visual cortex signals was impacted by SCDi in a genotype-dependent manner. Indeed, WT mice receiving SCDi showed a significantly less negative D in comparison to WT mice receiving vehicle while the treatment did not significantly impact D in 3xTg mice that are already showing a less negative D (Fig. 3D to 3F, last row; Table S1C). This effect was not modulated by time-of-day (Fig. 3D, last row of second column; Table S1C). Overall, analyses of D reveal state-specific changes, indicative of more fractal dispersion (more multifractality) during wake in 3xTg mice, and less dispersion during PS after SCDi treatment in WT mice.

Hippocampal lipid droplet (LD) alterations in 3xTg mice mitigated by SCDi

The SCDi treatment was previously shown to reduce MUFA-enriched triglycerides specifically in the mouse subventricular zone (Hamilton et al., 2015). Here, quantitative lipid profiling was conducted on left hemispheres to assess the general/brain-wide effect of the treatment on MUFAs and saturated fatty acids (SFAs), and potential associations with wake/sleep phenotypes. This quantification confirmed elevated MUFA-enriched and/or MUFA to SFA ratio for triglycerides and phospholipids combined with free fatty acids in 3xTg mice in comparison to WT mice (i.e., palmitoleic acid and palmitoleic to palmitic acid ratio), accompanied by similar elevations in the SFA myristic acid (both triglycerides and phospholipids; Fig. 4A and Table S1D). Interestingly for triglycerides, and similar to Beta and Gamma activity during wake and PS, the inhibition of SCD was found to impact the level of SFAs in an opposite manner in 3xTg and WT mice. Indeed, the treatment resulted in a higher level of arachidic acid in 3xTg mice compared to WT mice, and rescued the diminished SFAs found in 3xTg mice treated with vehicle when considering a pool of low level SFAs (i.e., myristic acid, margaric acid, arachidic acid, behenic acid, lignoceric acid; Fig. 4A and Table S1D).

LDs were found to be increased specifically in the subventricular zone in 3xTg mice (Hamilton et al., 2015). The recent development of refined approaches to detect LDs in brain tissue (Petrelli et al., 2024) allowed the quantification of the combined effects of the mutation and SCD inhibition on LDs in the CA1 and CA3 regions of the hippocampus (*stratum pyramidale*), targeted to align with measurements of astrocytic markers. In CA1, the number of LDs per cell in 3xTg mice (vehicle) was higher than that of WT mice (vehicle), and was restored to WT level with SCDi (Fig. 4B and 4C, Fig. S5 and Table S1D; similar tendency when considering together LDs and clusters of LDs). In CA3, the number of LDs and clusters of LDs per cell was significantly lower in mutant mice in comparison to WT mice (both vehicle), and was significantly increased by SCDi in 3xTg animals only (Fig. 4B and 4C, Fig. S6 and Table S1D; similar tendency for LDs per cell). These findings point to a rescue effect of SCD inhibition on 3xTg-altered LDs in hippocampal regions. Furthermore, given the LD alterations in opposite directions in the CA1 and CA3 of mutant mice, the results underscore the importance of not using observations relative to a given brain region as a proxy for another brain region, even if functionally related.

Elevated GFAP-positive cell density in CA1 of 3xTg mice attenuated by SCDi

The number of cells expressing two well-recognized markers of astrocytes (and of astrocyte activation for GFAP) was investigated after SCD inhibition in WT and 3xTg mice. In the hippocampal CA1, SCDi treatment significantly restored the elevated GFAP-positive cell density in 3xTg mice (Fig. 5A and Table S1E). In CA3, GFAP-positive cell density was observed to be higher in 3xTg in comparison to WT mice, and SCDi did not significantly impact it (Fig. 5A and Table S1E), while for the DG, no significant difference between genotypes or treatments was found (Fig. S7A and Table S1E). These findings support an elevated number of GFAP-stained cells in the CA1 and CA3 regions of the hippocampus in 3xTg mice that can be rescued to WT values in CA1 by the inhibition of SCD.

Concerning the LH and targeted thalamic nuclei, the density of ALDH1L1-positive cells was also significantly elevated in 3xTg in comparison to WT mice (Fig. 5B and Table S1E). However, SCDi treatment did not affect ALDH1L1-positive cell density in these regions (Table S1E). The substantial effect of the AD-relevant mutations on ALDH1L1 staining in these sleep-related regulatory brain regions is thus not modulated by SCD inhibition, which is evocative of observations made for most wake/sleep variables.

The morphology of CA1 astrocytes was found to be modified by SCD inhibition in a manner independent of genotype. Indeed, the treatment significantly increased the radius size of the area covered by astrocytes, and showed a tendency to increase the mean length of astrocytic processes/branches, whereas these parameters were not significantly affected in 3xTg mice (Fig. 5C to 5E, and Table S1E). The total length of astrocytic processes/branches was not significantly modified by treatment and/or

genotype (Fig. S7B and Table S1E), which also applies to the number of branch intersections as a function of the distance from the soma (Fig. S7C and Table S1E). These observations suggest that the inhibition of SCD for at least 28 days modestly increases the length of individual astrocytic processes resulting in a generally larger diameter of coverage. In this region (i.e., CA1), the ALDH1L1 staining mainly appears in the form of small puncta (Fig. 5F). The number of ALDH1L1 puncta associated to GFAP-stained processes/branches and cell bodies was found to be significantly lower in 3xTg mice in comparison to WT mice, but was not significantly impacted by SCDi (Fig. 5G and Table S1E). Thus, SCD inhibition modulated astrocyte morphology, while genotype affected (independently of treatment) ALDH1L1 staining associated to astrocytes in the CA1 hippocampal region.

Transcriptomic alterations in different brain regions of 3xTg mice modified by SCDi

A spatial transcriptomic approach was used to identify potential molecular mechanisms underlying wake/sleep phenotypes in mutant mice and effects of SCDi. Whole-slide gene expression (i.e., all spatial spots [bulk]) was first considered for a slide covering the cerebral cortex, hippocampus, thalamus and hypothalamus (Fig. 6). Four different comparisons were performed: **1)** 3xTg versus WT mice both treated with vehicle (Genotype effect), **2)** WT mice with SCDi versus with vehicle (SCDi effect in WT), **3)** 3xTg mice with SCDi versus with vehicle (SCDi effect in 3xTg), and **4)** 3xTg versus WT mice both treated with SCDi (SCDi effect in 3xTg vs WT); identifying, respectively, 5,644 , 1,999, 604, and 641 DEGs (FDR < 0.05; Fig. 6A and Table S2). The gene set associated with the Genotype effect was submitted to KEGG pathway enrichment analysis, which confirmed a global impact of the 3xTg genotype on genes related to inflammation (e.g., 'autophagy', 'leukocyte transendothelial migration', 'TGF-beta signaling pathway', 'chemokine signaling' and 'phagocytosis'), oxidative stress ('oxidative phosphorylation') and neurodegeneration (Fig. 6B and Table S3). More precisely, the expression of inflammation-related genes was significantly higher across the whole slice in the 3xTg brain when compared to the WT brain as exemplified by *Cx3cl1*, *Thy1*, *Arrb1*, *Atp6v1g2* and *Tubb4a* (Fig. 6C). The expression of mitochondrial genes was found to be significantly lower in 3xTg relative to WT brain (e.g., *Mt-atp8*, *Mt-co3*), whereas that of *Klc2*, a gene coding for a protein involved in moving organelles across microtubules and part of the "neurodegeneration" KEGG pathway, was higher in the mutant brain (Fig. 6C). Interestingly, multiple signaling pathways were also significantly enriched in genes impacted by genotype (e.g., 'MAPK signaling pathway', 'cAMP signaling pathway', 'calcium signaling pathway' and 'mTOR signaling pathway'; Fig. 6B), suggesting modifications in a wide range of cellular functions in the brain of 3xTg-AD female mice. These observations validate the representativity of the current dataset and its suitability to identify AD-relevant gene networks.

Interestingly, genotype was linked to more DEGs than other comparisons, but there was a notable overlap with other lists of DEGs (Fig. 6D). To identify genes potentially rescued by SCDi in 3xTg mice among the 2,755 genes affected by SCDi across genotypes when considering the full brain slice, DEGs between the 3xTg and WT mice (vehicle) that were also differentially expressed between 3xTg mice receiving SCDi and vehicle were examined (Fig. 6D). Among genes identified with this strategy, *Aldh1a1*, *Cox6a2* and *Shank3* are featured in Fig. 6E, with the expression of the first two being decreased in 3xTg mice and increased by SCDi, and that of the last being increased in mutant mice and decreased by SCDi. *Aldh1a1* is of particular relevance because the protein product of this gene was shown to be involved in astrocyte differentiation (Adam et al. 2012), and to have roles in molecular mechanisms of neuroprotection and neurodegeneration (Nikhil et al. 2019). Moreover, SCD was found to regulate the expression of *Aldh1a1* in cancer cells (Sun et al. 2022). The expression of *Cox6a2* was also reported to be decreased in the hypothalamus of another AD mouse model (Liu et al. 2023), and a variant in this gene was linked to AD risk in humans (Teerlink et al. 2022). *Shank3* codes for a scaffolding protein predominantly localized at excitatory synapses, which level is altered in humans diagnosed with AD (Wan et al., 2021; Landry et al., 2023). Together, these observations provide further support to a potential use of SCDi to alleviate specific AD-related dysfunctions as proposed previously (Hamilton et al., 2022).

Importantly, spatial transcriptomics allows to simultaneously interrogate gene expression signatures of multiple brain regions. Spatial clusters were generated using automatic clustering and the four brain slices (of the four experimental groups; Fig. S8A). These clusters were then used to manually assign spatial spots to the cerebral cortex, hippocampus, thalamus and hypothalamus for each comparison, which resulted in a considerable overlap in the distribution of gene expression patterns for all regions (Fig. S8B and S8C). For the cerebral cortex, 264 DEGs were identified for the Genotype effect, 167 for SCDi effect in WT mice, 15 for SCDi effect in 3xTg mice, and 13 genes for SCDi effect in 3xTg versus WT mice (Fig. S9A, Table S4). For the hippocampus, 112 DEGs were found for the Genotype effect, 66 for SCDi effect in WT, 16 for SCDi effect in 3xTg, and 28 for SCDi effect in 3xTg versus WT mice (Fig. S9A, Table S5). For the thalamus, 244 DEGs were found for the Genotype effect, 86 for SCDi effect in WT, 45 for SCDi effect in 3xTg, and 15 for SCDi effect in 3xTg versus WT mice (Fig. S9A, Table S6). Finally, for the hypothalamus, 87 DEGs were observed for the Genotype effect, 99 for SCDi effect in WT, 123 for SCDi effect in 3xTg, and 19 for SCDi effect in 3xTg versus WT mice (Fig. S9A, Table S7). Pathway enrichment analysis was conducted on lists of DEGs representing the Genotype effect for each region to identify impacts of the mutation on molecular functions, biological processes and KEGG pathways (Fig. 7A, Table S8). Gene networks related to the immune system were found to be particularly affected in the hippocampus, those linked to glial cells to be affected in the cerebral cortex and hippocampus, and those linked to synapse function and neuronal plasticity in the cerebral cortex,

hippocampus and thalamus. Concerning the hypothalamus, enriched pathways comprising many genes were generally linked to neuropeptide signaling, protein and DNA binding, and transcription. However, the expression level of a number of these genes could be affected by the antero-posterior position of the slice that slightly differed between genotypes. These pathways were thus not illustrated but are listed in Table S8D.

Overall, the 3xTg-AD model was found to drive notable brain region-specific effects. For instance, the expression of *Lamc2* and *Tnnc1* (gene ontology terms 'extracellular matrix' and/or 'motor proteins') was only significantly higher in 3xTg mice compared to WT mice (both vehicle) in the cerebral cortex, that of *Gfap* ('neuron projection development' and 'astrocyte development'), *Parp* ('transferase activity') and *C1qa* ('innate immune response', 'synapse pruning' and 'prion disease') was higher in 3xTg relative to WT mice specifically for the hippocampus, and that of *Ighm* ('innate immune response') significant for both the cerebral cortex and hippocampus (Fig. 7B). In addition, the expression of *Syn1* ('synapse organization' and 'short-term plasticity'), *Arrb1* ('negative regulation of apoptosis' and 'MAPK signaling pathway'), *Cacng2* ('ion transmembrane transport' and 'neurotransmitter receptor internalization') and *Gabra3* ('neurotransmitter receptor internalization' and 'MAPK signaling pathway') was only significantly higher in 3xTg compared to WT mice for the thalamus (Fig. 7B). Finally, the expression of *Aldh7a1* ('oxidoreductase activity') was significantly higher in the mutant thalamus and hypothalamus, whereas that of *Rgcc* ('protein binding' and 'negative regulation of cell population proliferation') was significantly lower in the mutant cortex, hippocampus and hypothalamus (Fig. 7B). These observations of brain region-specific effects of the 3xTg genotype were made possible by the use of spatial transcriptomics.

To identify genes that are rescued by SCDi in the targeted brain regions, fold changes in expression across the four different comparisons (including DEGs found in at least one of the four comparisons) were clustered (ward.D2) to unveil patterns of directional changes (Fig. S9B). However, this led to very few patterns of directional changes associated to DEGs in different comparisons. Therefore, clustering was then conducted with DEGs found for the Genotype effect or the SCDi effect in 3xTg mice (two comparisons only), which revealed four main clusters (Fig. 7C, Table S9A). These are mainly comprised of genes with lower expression in 3xTg compared to WT mice (both vehicle) for which the expression is higher in 3xTg mice treated with SCDi compared to vehicle, and genes with the opposite pattern (higher expression in 3xTg than WT mice vehicle and lower in 3xTg with SCDi than vehicle; Fig. S9C). Few genes per region were significantly modified for both comparisons with a substantial degree of overlap between regions (Table S9B). Among these, the expression of *Hddc3* (coding for a protein involved in ferroptosis; Ding et al., 2020; Lin et al., 2021) was significantly lower in mutant and rescued by SCDi in all four regions; the same was observed for *Pdyn* expression in the hypothalamus, while

Fam81a (protein product regulating synapse organization; Kaizuka et al., 2024) showed an opposite pattern in the thalamus (Fig. 7D and Fig. S10). Therefore, the inhibition of SCD in 3xTg-AD mice generally impacts the transcriptome in a 'brain-wide' manner and could rescue some of the gene expression changes found in mutant females in multiple brain regions.

Hippocampal subregions (CA1, CA3 and DG) were also examined for the effect of genotype and SCDi on the transcriptome. These subregions could adequately be identified on spatial maps, and showed distinct distributions of gene expression patterns that overlapped between experimental groups (Fig. S11A and S11B). This strategy identified 31 DEGs for the Genotype effect in CA1, 15 in CA3 and 49 in DG (Fig. S11C, Table S10). Some of these genes were rescued following SCDi treatment, notably *Ifi27l2a* in CA1, and *Tac2* and *Pmch* in the DG (Fig. S11D), which were represented given their role in the immune system, stress responses, and sleep regulation (Hook et al., 2019; Calafate et al., 2023; Kim et al., 2023). These analyses provide additional support to an important effect of the 3xTg genotype on hippocampal gene expression as well as to a potential therapeutic effect of SCDi as highlighted previously using single cell transcriptomics focused on microglia (Hamilton et al., 2022).

DISCUSSION

We have here uncovered that targeting lipid metabolism using the inhibition of SCD is not noticeably correcting the wide range of modifications in wake/sleep variables found in 3xTg-AD mice. However, we discovered that this lipid metabolism-targeting treatment mitigates the impact of the mutant on brain lipids, LDs and astrocytes in the hippocampus, and the transcriptome of different brain areas. The overall findings, summarized in Table 1, could suggest that the ameliorations of brain lipids, hippocampal glia and brain gene expression are not sufficient to revert major wake/sleep alterations (at least in relatively young 3xTg-AD female mice). Furthermore, the research will help clarifying the complex relationship between lipids, glial cells and sleep, and how the inhibition of SCD shows promise in reverting multiple cellular and molecular modifications in the context of neurodegenerative conditions.

Our comprehensive investigation of wake/sleep phenotypes has allowed to refine previous observations in 3xTg-AD mice in addition to identifying novel features characterizing this model. Firstly, we found that 5-month old mutant animals sleep more during the dark (active) period, which is in line with findings using a piezoelectric evaluation in 16-month old females (Saber et al., 2021). Our data indicate that this is specifically linked to more time spent in SWS. However, no change in time spent awake and asleep was found in 18-month old 3xTg mice when considering the two sexes (i.e., 4 females and 4 males; Kent et al., 2018), which could indicate a sex-specific effect or an effect that can be captured

only at a younger age. More sleep during the active period in 3xTg-AD females is reminiscent of the lower amplitude of the wake/sleep cycle in AD patients comprising a higher incidence of daytime naps (Wang and Holtzman, 2020; Kent et al., 2021), but differs from several other transgenic mouse models that generally show more time spent awake and less time asleep (Dufort-Gervais et al., 2019). Given the reported wake-promoting role of LH astrocytes (Clasadonte et al., 2017; Cai et al., 2022), alterations in astrocytic function in the LH could be a factor contributing to the diminished wake amount in 3xTg-AD mice. Our observation of an elevated number of ALDH1L1-positive cells in the LH could indeed suggest an impaired function of astrocytes (e.g., sign of abnormal compensation or of overactivation) preventing these cells from effectively promoting wake.

Secondly, we exposed multiple alterations in ECoG rhythmic and scale-free activity that encompass different cortical areas in the selected AD model. Indeed, absolute power was globally reduced (i.e., all states) and a redistribution of the contribution of activity in different frequencies in favor of a higher contribution of faster frequencies (particularly manifest for SWS and pointing to a decreased quality of SWS) was characterizing adult 3xTg-AD female mice, together with more anti-persistent scale-free activity (wake and SWS). These findings could be specific for the targeted age and sex because an absence of change in ECoG relative activity of the three vigilance states for similar cortical regions was reported in 3xTg-AD mice at 18 months when considering the two sexes together (Kent et al., 2018). The reduction of absolute power could be considered consistent with the reduced number of sleep oscillations (i.e., spindles and sharp-wave ripples) previously reported for this model after a learning task (Benthem et al., 2020). In addition, more anti-persistent ECoG multifractal activity may indicate a less organized/coordinated neuronal network in 3xTg-AD mice, which is also supported by observations of impaired hippocampal-parietal and delta-spindle coupling after learning (Benthem et al., 2020). Our findings are suggestive of an overall increased scale-free complexity in mutant mice. Given that reports in AD patients using related metrics are most often indicative of a decreased arrhythmic/fractal complexity of the electroencephalogram (Lau et al., 2022; Averna et al., 2023), it is interesting to note that the deviation from the ‘optimal range’ in the complexity of electroencephalographic activity has been proposed to be a more suitable variable to use for clinical applications in comparison to the directionality of the changes (Lau et al., 2022). It is anticipated that a decrease in dendritic spine density in the targeted cortical areas or other types of synaptic dysfunctions, as reported for the hippocampus in this model (Dufort-Gervais et al., 2020; Hamilton et al., 2022), are contributing to the extensive modifications in ECoG rhythmic and arrhythmic activity in 3xTg-AD animals. Our findings of major alterations in the transcriptome of the cerebral cortex in particular, notably linked to glial cell functioning, cell adhesion and neuronal plasticity, also offer mechanisms by which ECoG activity can be modified in mutant mice.

Our hypothesis that the inhibition of SCD could rescue wake/sleep alterations in 3xTg-AD mice (via a mechanism implicating astrocytes) was not confirmed by data resulting from wake/sleep phenotyping. SCDi did not markedly impact wake/sleep architecture variables, but did modify ECoG rhythmic activity in a genotype-dependent way. Predominantly during PS (and also during wake), SCDi appears to reduce fast ECoG rhythmic activity (and multifractal dispersion) in WT mice, whereas it increases that of 3xTg-AD mice. This implies that this treatment can modulate wake/sleep quality, and in a manner that depends on how the brain is wired and affected by AD-related pathology. Indeed, in a normal brain with preserved lipid metabolism, interfering with the production of MUFAs using SCD inhibition is expected to have an impact that will differ from that in a brain for which the pathology shifted lipid balance and increased MUFAs. In mutant mice, the inhibition of SCD could impact ECoG activity via changing synaptic strength since it was found to affect the density of dendritic spines in the hippocampus specifically in this model (Hamilton et al., 2022). In parallel, SCDi could modulate the ECoG by altering fatty acid concentration/composition because fatty acid administration and the activation of a fatty acid receptor were shown to affect neuronal firing (Arsenault et al., 2011; Barki et al., 2022). Interestingly, the whole-brain level of specific SFAs (i.e., triglycerides), was also found to be changed in opposite directions in mutant and WT mice, which could support a contribution to opposite effects on ECoG rhythms. Additionally, SCDi impact on the expression of *Pmch* in the hippocampus could represent another mechanism since this gene codes for melanin-concentrating hormone (MCH), which was proposed to contribute to sleep disturbances in an AD mouse model (Calafate et al., 2023). Despite the very few available studies investigating the direct impact of lipids on wake/sleep quality, it is of interest to observe that SCD effects on ECoG activity were dependent on wake/sleep state, which suggest effects on state-specific regulatory cell populations. More research has rather focused on the impact of sleep disturbances on lipids (Bell et al., 2013; Broussard et al., 2015; Haynes et al., 2024). In fact, sleep deprivation was shown to increase markers of SCD activity in the serum of healthy young men (Skuladottir et al., 2016). Accordingly, disturbed sleep could contribute to elevated MUFAs in the AD brain, and inhibiting SCD may represent a way to counteract the effect of sleep disturbances in AD.

As presented in the introduction, astrocytes are in a key position to mediate a relationship between wake/sleep states and lipid metabolism, notably given their major roles in LD formation and homeostasis and their expression of SCD (Batiuk et al., 2020; Smolič et al., 2021; Bedoya-Guzmán et al., 2023; Petrelli et al., 2024). Previous work reported changes in astrocytes in 3xTg-AD mice that depend on brain regions. Indeed, increased GFAP staining (i.e., fluorescence intensity) and other indications of astrocytic hyperreactivity have been reported in primary cell cultures from the 3xTg-AD cerebral cortex (González-Molina et al., 2021), while atrophic astrocytes were found in the entorhinal cortex of 3xTg mice starting at one month of age (Yeh et al., 2011), and signs of atrophy reported for the DG at different ages together

with no change in the number of stained astrocytes (Olabarria et al., 2010). Effects of normal aging on astrocytes in mice were also reported to be highly different between brain regions (i.e., GFAP-derived hypertrophy with age in hippocampal regions but atrophy in entorhinal cortex; Rodríguez et al., 2014). Our findings are consistent with this brain region-dependency and emphasize the need to use various markers to interrogate different subpopulations of astrocytes. Globally, we report a higher number of cells expressing GFAP and ALDH1L1 in hippocampal regions and LH/thalamus, respectively, a higher *Gfap* gene expression in the hippocampus, and an absence of detectable change in GFAP-derived morphology in 3xTg-AD females. It is interesting to point out that a lower number of ALDH1L1 puncta on GFAP-expressing cell was also observed in mutant mice. Diffuse expression of ALDH1L1 has been reported previously in the mouse hippocampus (Lowery et al., 2021). Knowing the role of this enzyme in cellular energy metabolism/mitochondrial function, this observation provides an additional indication of an altered astrocytic function in the studied model.

Importantly, we found the inhibition of SCD to reduce the number of CA1 cells expressing GFAP in mutant mice. Additional support for effects of SCDi treatment on astrocytes comes from findings regarding *Aldh1a1* and LDs. Fatty acids could be part of the mechanism by which SCDi reduces GFAP-positive cell count in CA1 in the studied AD model. Astrocytes were shown to respond to neuron-derived fatty acids by forming LDs (Ioannou et al., 2019), and 3xTg-AD mice have been reported to have an increased number of LDs in the subventricular zone (Hamilton et al., 2015), in addition to a higher LD number in CA1 in the current study. This could be associated with a higher metabolic demand on astrocytes. Since the inhibition of SCD was found to reduce AD-associated triglycerides in the subventricular zone (Hamilton et al., 2015), and to reduce LDs in CA1, it could contribute to a reduction in the need for metabolically active astrocytes to deal with lipids, and consequently to the lowered number of GFAP-expressing cells. A regulatory role of SCD on CA1 astrocyte function is also supported by the findings of a larger area covered by astrocytes under SCD inhibition (increased radius indicative of hypertrophy in both WT and 3xTg-AD mice), which might represent extension of cell processes in response to altered lipid availability. Lipid- and SCD-mediated changes of astrocytic function could in parallel impact their regulatory role in synaptic plasticity (Murphy-Royal et al., 2020), of relevance to the regulation of wake/sleep states. However, changes in hippocampal astrocytes under treatment seem to depart from wake/sleep phenotypes, and mechanisms are likely highly dependent on brain regions (as raised above). Indeed, in CA3, SCDi did not rescue the elevated number of GFAP-expressing cells in mutant mice, but rescued the number of LDs that was lower (and not elevated as in CA1). Astrocytes in CA1 and CA3 were also previously reported to respond differently to an AD-related genetic manipulation (Ugolini et al., 2018). Given that the CA3 region is differently wired in comparison to CA1 (Cherubini and Miles, 2015), differences between regions in how astrocytes contribute to lipid metabolism and

respond to lipid-modifying treatments are anticipated.

The transcriptome of the cerebral cortex, the hippocampus, the thalamus and hypothalamus was found to be importantly impacted in 3xTg-AD female mice, in particular concerning gene networks linked to inflammation and immune system, glial cell functioning, and neuronal plasticity. This aligns with previous observations made separately for different brain regions in this transgenic model (Hamilton et al., 2022; Jiang et al., 2023; Widjaya et al., 2023; Barber et al., 2024), and also with recent finding of transcriptomic changes across different layers of the frontal/prefrontal cortex in AD patients, especially with regard to inflammatory pathways and glial functions (Miyoshi et al., 2024; Wang et al., 2024). The current findings distinguish themselves by the high throughput and simultaneous interrogation of multiple brain regions in the targeted AD model that has enabled the identification of both whole-brain and region-specific effects. As emphasized above, a number of these gene expression changes can contribute to the marked alterations in wake/sleep ECoG activity (e.g., *Pmch*, see Calafate et al., 2023). Together with our observations related to astrocytes, the expression of microglia-specific genes was reported to be altered in the hippocampus of 3xTg-AD mice (Hamilton et al., 2022), which supports changes to diverse glial populations in the hippocampus of this model. Given the recently reported association of *Ifi27l2a* with microglial function (Kim et al., 2023), our finding of higher *Ifi27l2a* expression in hippocampal subregions of mutant mice provides further support to changes in microglia functioning in this AD model. Moreover, the observation that this high *Ifi27l2a* expression is reduced by treatment in mutant mice similarly aligns with an effect of SCD inhibition on microglia as exposed previously (Hamilton et al., 2022). Microglia, similar to astrocytes, can contribute to mechanisms linking lipid alterations to wake/sleep phenotypes given the accumulated findings supporting their role in both the control of lipid metabolism and the regulation of sleep (Goodman et al., 2024; Ma et al., 2024).

In general, the current data are supporting previous observations of positive effects of SCDi in rescuing gene expression patterns in 3xTg-AD mice (Hamilton et al., 2022), and expand this observation to regions other than the hippocampus. This indicates that lipid metabolism, at least related to SCD, has a notable effect on the regulation of gene expression in the mouse brain. This is also exemplified by the substantial effect of SCDi on the transcriptome in WT mice, even if this effect was not focused on in the presented analyses. Indeed, when considering the two genotypes, 2,755 genes were altered by the inhibition of SCD, which could originate, at least in part, from a direct effect on astrocytes given their expression of SCD (Batiuk et al., 2020; Bedoya-Guzmán et al., 2023). One can also speculate that the altered fatty acid profile will drive changes in the activity of several transcription factors across different cell types to contribute to modifications of the transcriptome (e.g., peroxisome proliferator–activated receptors having fatty acids as ligands). In the current study, the presentation of data has mostly focused on restricted gene sets that may be of particular relevance to the rescuing effect of SCD inhibition.

Nevertheless, given that a brain with major pathological features could benefit from changes/compensations departing from the normal state, considering the more global effect of the treatment in the disease model, including less frequent genes with expression further departing from the 'normal' level after treatment in addition to targets restored to levels closer to WT, could be relevant to fully capture the therapeutic potential of SCD inhibition.

A first limitation of the present study concerns the use of female mice only, which limits the generalizability of the findings. This choice was guided by the more severe amyloid β pathology reported in female 3xTg mice in comparison to males (Hirata-Fukae et al., 2008; Barber et al., 2024), and by the higher risk of developing AD/higher AD prevalence in women (Cao et al., 2020; Gustavsson et al., 2023; Lautenschlager et al., 1996). However, sex differences in sleep phenotypes exist (Dib et al., 2021), and recent data indicate a higher efficiency of AD-targeting treatments in men in comparison to women (Kurkinen, 2023). Accordingly, future investigations of sleep after SCD inhibition or related interventions should also include males. Secondly, even if justified from previous research (Hamilton et al., 2015, 2022), the present study has solely evaluated the impact of a 28-day (nominal) treatment administered at a relatively early age (approximately four months). It is possible that longer treatments as well as treatment targeting an age range with milder wake/sleep alterations could have resulted in some level of rescue of wake/sleep variables. Given that lipid alterations are found at two months in the model studied (Hamilton et al., 2015), treating before this age could be considered. However, there is indications for the gene expression landscape of the hippocampus in 3xTg mice to be more impacted in animals of 12 months (Ochi et al., 2020), which could also justify studying the effects of the treatment in older mice. In addition, a single concentration of SCDi was used in the present study (i.e., 80 μM) and, although within the range of doses shown to have positive effects on AD-related phenotypes in 3xTg female mice (Hamilton et al., 2015, 2022), testing the efficacy of a range of doses in the context of wake/sleep evaluation would be an important next step. It should be noted that ECoG activity was interrogated for regions of the cerebral cortex while astrocytes were examined in the hippocampus, LH, and thalamic nuclei. This methodological choice was made to simultaneously capture sleep regulatory regions (e.g., LH) and the hippocampus, because of the previously described modifications of hippocampal astrocytes in 3xTg-AD mice (Olabarria et al., 2010, 2011), and the reported effects of SCD inhibition on hippocampal cell populations (Hamilton et al., 2015, 2022). Although the LH and hippocampus can shape ECoG activity during wake/sleep states, future work should interrogate astrocyte and microglia functioning at the site of ECoG recording.

In parallel, the LD staining used was previously shown to label LDs containing the protein perilipin 2 with a high level of specificity (Petrelli et al., 2024), but LDs lacking perilipin 2 could be impacted differently by the mutations and treatment. Perilipin 2 remains a well established marker of LD

(Madsen et al., 2024), and the use of transgenic mice expressing this protein tagged with a fluorescent reporter will likely be needed to identify the specific cell type in which LDs were changed in 3xTg-AD mice and under the inhibition of SCD. Indeed, even if astrocytes appear to contain more LDs than neurons and that astrocytic LDs respond more than neuronal LDs to amyloid β oligomers characterizing AD (Madsen et al., 2024; Zhang et al., 2025), the impact of 3xTg and SCDi specifically on astrocytes LDs remains to be established. This could be achieved by crossing different transgenic mouse lines given the challenge of combining dye-mediated LD detection and IHC (to stain specific cell types) related to the notable influence of tissue processing methodology and detergent use on the capacity to detect LDs (Petrelli et al., 2024). Lastly, there was some variability between experimental groups in the exact antero-posterior localization of the brain slice used for spatial transcriptomics, and only one brain slice per experimental group was interrogated given budget availability. The slight variability was observed to have a potential effect on gene expression particularly for the hypothalamus and thalamus for which findings should be interpreted with caution. While some of the results are validated by other observations (e.g., hippocampal *Gfap*) and that molecular and cellular functions identified from gene expression changes in mutant mice and driven by treatment show a good correspondence with the literature (e.g., inflammation and immune system, glial cell functioning, and neuronal plasticity matching Hamilton et al., 2022; Jiang et al., 2023; Widjaya et al., 2023; Barber et al., 2024; Miyoshi et al., 2024; Wang et al., 2024), replication of spatial transcriptomic findings will be needed.

CONCLUSIONS

The present dataset highlights an extensive range of modifications in wake/sleep architecture and ECoG quality as well as in lipids, astrocytes and the transcriptome of different brain regions in a widely used mouse model of AD. This includes the original finding of higher multifractal complexity during wakefulness and SWS in (relatively young) 3xTg-AD female mice, which has a high relevance to the understanding of mechanisms underlying the development of impaired cognitive functioning in neurodegenerative diseases (Averna et al., 2023). The changes in wake/sleep phenotypes were not restored to WT values by the inhibition of SCD, whereas a number of lipidic, astrocytic and gene expression changes were. Nonetheless, we have identified effects of SCD inhibition on ECoG signatures of wake/sleep states, pointing to a role of lipid metabolism in the regulation of synchronized cerebral cortex activity during wakefulness and sleep. SCD inhibition was previously found to reduce the activation of microglia in the 3xTg-AD model (Hamilton et al., 2022), and in combination with our current findings regarding the astrocytic marker GFAP, LDs and transcriptomic changes associated to

glial cells and immune function, these discoveries collectively suggest that glial populations are important targets of this intervention. Future research could evaluate how the different astrocytic functions, assembled recently in a framework as a contextual guide/integrator (Murphy-Royal et al., 2023), are contributing to lipid-dependent changes in wake/sleep quality using, for instance, manipulations of specific lipid metabolism-related enzymes in astrocytes.

DECLARATIONS

Authors' contributions

A.H., K.F., J.B., and V.M. designed the experiments and analytic plan. A.H. and J.D.-G. performed the animal experiments. A.H. and T.L. analyzed the electrophysiological and transcriptomic data. A.H. and M.J.d.C.C. conducted IHC experiments and analyses. B.D.-L. provided assistance with IHC and spatial transcriptomics, and conducted LD measurements. A.H., T.L., M.J.d.C.C. and V.M. performed statistical analyses and graphical representations. C.B. and J.-M.L. produced the code for scale-free activity analysis. C.D. and C.D.R. conducted fatty acid quantification and interpretation. A.H., T.L., M.J.d.C.C., and V.M. wrote and revised the manuscript. V.M. supervised all experiments and analyses. A.H., M.J.d.C.C., T.L., K.F., J.B., and V.M. provided funding. All authors approved the final version of the manuscript.

Conflict of interest

The authors have no conflict of interest to declare.

Data availability

Transcriptomic data are available at the GEO repository under accession number GSE275131. All other data are included in this article and its supplementary file. Raw data are available from the corresponding author upon reasonable request.

Acknowledgements

The authors are thankful to Laura Hamilton, Lewis Rhys Depaauw-Holt and Ciaran Murphy-Royal for help and advice related to experiment and interpretation. The authors also want to thank Aurélie Cleret-Buhot from the cellular imaging platform of the Centre de recherche du Centre hospitalier de l'Université de Montréal (CRCHUM) for precious help with the development of the microscopy pipeline, Véronique Barrès and Liliane Meunier from the molecular pathology platform (CRCHUM) for help with acquisition

of histology images related to spatial transcriptomics, and Marie-Claude Therrien from the animal facility (CRCHUM) for assistance with animal transfer. Finally, the authors thank the staff from the Centre d'expertise et de services of Génome Québec (in particular Geneviève DonPierre) for sharing their expertise in RNA sequencing.

Funding

The research has been funded by a grant from the Canadian Institutes of Health Research to J.B. and V.M. (#437413), the Canada Research Chair in Sleep Molecular Physiology (V.M.), a scholarship from the Fonds de recherche du Québec - Santé (A.H.; #304560), a scholarship from the Natural Sciences and Engineering Research Council of Canada (T.L.; #569233-2022), and scholarships from the University of Groningen (M.J.d.C.C.).

REFERENCES

Adam SA, Schnell O, Pöschl J, Eigenbrod S, Kretzschmar HA, Tonn JC, Schüller U. 2012. ALDH1A1 is a marker of astrocytic differentiation during brain development and correlates with better survival in glioblastoma patients. Brain Pathol. 22(6), 788-797. https://doi.org/10.1111/j.1750-3639.2012.00592.x.

Adler P, Mayne J, Walker K, Ning Z, Figeys D. 2019. Therapeutic targeting of casein kinase 1δ/ε in an Alzheimer's disease mouse model. J. Proteome Res. 18, 3383-3393. https://doi.org/10.1021/acs.jproteome.9b00312.

Areal CC, Cao R, Sonenberg N, Mongrain V. 2020. Wakefulness/sleep architecture and electroencephalographic activity in mice lacking the translational repressor 4E-BP1 or 4E-BP2. Sleep 43, zsz210. https://doi.org/10.1093/sleep/zsz210.

Areal CC, Lemmetti N, Leduc T, Bourguignon C, Lina JM, Bélanger-Nelson E, Mongrain V. 2025. The absence of Neuroligin-1 shapes wake/sleep architecture, rhythmic and arrhythmic activities of the electrocorticogram in female mice. Mol. Brain, in press.

Arsenault D, Julien C, Tremblay C, Calon F. 2011. DHA improves cognition and prevents dysfunction of entorhinal cortex neurons in 3xTg-AD mice. PLoS One 6, e17397. https://doi.org/10.1371/journal.pone.0017397.

Astarita G, Jung KM, Vasilevko V, Dipatrizio NV, Martin SK, Cribbs DH, Head E, Cotman CW, Piomelli D. 2011. Elevated stearoyl-CoA desaturase in brains of patients with Alzheimer's disease. PLoS One 6, e24777. https://doi.org/10.1371/journal.pone.0024777.

Averna A, Coelli S, Ferrara R, Cerutti S, Priori A, Bianchi AM. 2023. Entropy and fractal analysis of brain-related neurophysiological signals in Alzheimer's and Parkinson's disease. J. Neural Eng. 20, 051001. https://doi.org/10.1088/1741-2552/acf8fa.

Ballester Roig MN, Leduc T, Dufort-Gervais J, Maghmoul Y, Tastet O, Mongrain V. 2023. Probing pathways by which rhynchophylline modifies sleep using spatial transcriptomics. Biol. Direct. 18, 21. https://doi.org/10.1186/s13062-023-00377-7.

Barber AJ, Del Genio CL, Swain AB, Pizzi EM, Watson SC, Tapiavala VN, Zanazzi GJ, Gaur AB. 2024. Age, sex and Alzheimer's disease: a longitudinal study of 3xTg-AD mice reveals sex-specific disease

trajectories and inflammatory responses mirrored in postmortem brains from Alzheimer's patients. Alzheimers. Res. Ther. 16(1), 134. https://doi.org/10.1186/s13195-024-01492-x.

Barki N, Bolognini D, Börjesson U, Jenkins L, Riddell J, Hughes DI, Ulven T, Hudson BD, Ulven ER, Dekker N, Tobin AB, Milligan G. 2022. Chemogenetics defines a short-chain fatty acid receptor gut-brain axis. Elife. 11, e73777. https://doi.org/10.7554/eLife.73777.

Batiuk MY, Martirosyan A, Wahis J, de Vin F, Marneffe C, Kusserow C, Koeppen J, Viana JF, Oliveira JF, Voet T, Ponting CP, Belgard TG, Holt MG. 2020. Identification of region-specific astrocyte subtypes at single cell resolution. Nat. Commun. 11, 1220. https://doi.org/10.1038/s41467-019-14198-8.

Bedoya-Guzmán FA, Pacheco-Herrero M, Salomon-Cruz ID, Barrera-Sandoval AM, Gutierrez Vargas JA, Villamil-Ortiz JG, Villegas Lanau CA, Arias-Londoño JD, Area-Gomez E, Cardona Gomez GP. 2023. BACE1 and SCD1 are associated with neurodegeneration. Front. Aging Neurosci. 15, 1194203. https://doi.org/10.3389/fnagi.2023.1194203.

Belfiore R, Rodin A, Ferreira E, Velazquez R, Branca C, Caccamo A, Oddo S. 2019. Temporal and regional progression of Alzheimer's disease-like pathology in 3xTg-AD mice. Aging Cell. 18, e12873. https://doi.org/10.1111/acel.12873.

Bell LN, Kilkus JM, Booth JN 3rd, Bromley LE, Imperial JG, Penev PD. 2013. Effects of sleep restriction on the human plasma metabolome. Physiol. Behav. 122, 25-31. https://doi.org/10.1016/j.physbeh.2013.08.007.

Benthem SD, Skelin I, Moseley SC, Stimmell AC, Dixon JR, Melilli AS, Molina L, McNaughton BL, Wilber AA. 2020. Impaired hippocampal-cortical interactions during sleep in a mouse model of Alzheimer's disease. Curr. Biol. 30, 2588-2601.e5. https://doi.org/10.1016/j.cub.2020.04.087.

Billings LM, Oddo S, Green KN, McGaugh JL, LaFerla FM. 2005. Intraneuronal Abeta causes the onset of early Alzheimer's disease-related cognitive deficits in transgenic mice. Neuron 45, 675-688. https://doi.org/10.1016/j.neuron.2005.01.040.

Broussard JL, Chapotot F, Abraham V, Day A, Delebecque F, Whitmore HR, Tasali E. 2015. Sleep restriction increases free fatty acids in healthy men. Diabetologia 58, 791-798. https://doi.org/10.1007/s00125-015-3500-4.

Cai P, Huang SN, Lin ZH, Wang Z, Liu RF, Xiao WH, Li ZS, Zhu ZH, Yao J, Yan XB, Wang FD, Zeng SX, Chen GQ, Yang LY, Sun YK, Yu C, Chen L, Wang WX. 2022. Regulation of wakefulness by astrocytes in the lateral hypothalamus. Neuropharmacology 221, 109275. https://doi.org/10.1016/j.neuropharm.2022.109275.

Calafate S, Özturan G, Thrupp N, Vanderlinden J, Santa-Marinha L, Morais-Ribeiro R, Ruggiero A, Bozic I, Rusterholz T, Lorente-Echeverría B, Dias M, Chen WT, Fiers M, Lu A, Vlaeminck I, Creemers E, Craessaerts K, Vandenbempt J, van Boekholdt L, Poovathingal S, Davie K, Thal DR, Wierda K, Oliveira TG, Slutsky I, Adamantidis A, De Strooper B, de Wit J. 2023. Early alterations in the MCH system link aberrant neuronal activity and sleep disturbances in a mouse model of Alzheimer's disease. Nat. Neurosci. 26(6), 1021-1031. https://doi.org/10.1038/s41593-023-01325-4.

Cao Q, Tan CC, Xu W, Hu H, Cao XP, Dong Q, Tan L, Yu JT. 2020. The prevalence of dementia: a systematic review and meta-analysis. J. Alzheimers Dis. 73, 1157-1166. https://doi.org/10.3233/JAD-191092.

Chan RB, Oliveira TG, Cortes EP, Honig LS, Duff KE, Small SA, Wenk MR, Shui G, Di Paolo G. 2012. Comparative lipidomic analysis of mouse and human brain with Alzheimer disease. J. Biol. Chem. 287, 2678-2688. https://doi.org/10.1074/jbc.M111.274142.

Chatterjee P, Lim WL, Shui G, Gupta VB, James I, Fagan AM, Xiong C, Sohrabi HR, Taddei K, Brown BM, Benzinger T, Masters C, Snowden SG, Wenk MR, Bateman RJ, Morris JC, Martins RN. 2016. Plasma phospholipid and sphingolipid alterations in Presenilin1 mutation carriers: a pilot study. J. Alzheimers Dis. 50, 887-894. https://doi.org/10.3233/JAD-150948.

Chen ZP, Wang S, Zhao X, Fang W, Wang Z, Ye H, Wang MJ, Ke L, Huang T, Lv P, Jiang X, Zhang Q, Li L, Xie ST, Zhu JN, Hang C, Chen D, Liu X, Yan C. 2023. Lipid-accumulated reactive astrocytes

promote disease progression in epilepsy. Nat. Neurosci. 26, 542–554. https://doi.org/10.1038/s41593-023-01288-6.

Cherubini E, Miles R. 2015. The CA3 region of the hippocampus: how is it? What is it for? How does it do it? Front. Cell. Neurosci. 9, 19. https://doi.org/10.3389/fncel.2015.00019.

Ciuciu P, Abry P, Rabrait C, Wendt H. 2008. Log-wavelet Leaders cumulant based multifractal analysis of EVI fMRI time series: Evidence of scaling in ongoing and evoked brain activity. IEEE J. Sel. Top. Signal Process. 2, 929–943. https://doi.org/10.1109/JSTSP.2008.2006663.

Clasadonte J, Scemes E, Wang Z, Boison D, Haydon PG. 2017. Connexin 43-mediated astroglial metabolic networks contribute to the regulation of the sleep-wake cycle. Neuron 95, 1365-1380.e5. https://doi.org/10.1016/j.neuron.2017.08.022.

Dib R, Gervais NJ, Mongrain V. 2021. A review of the current state of knowledge on sex differences in sleep and circadian phenotypes in rodents. Neurobiol. Sleep Circadian Rhythms 11, 100068. https://doi.org/10.1016/j.nbscr.2021.100068.

Ding CC, Rose J, Sun T, Wu J, Chen PH, Lin CC, Yang WH, Chen KY, Lee H, Xu E, Tian S, Akinwuntan J, Zhao J, Guan Z, Zhou P, Chi JT. 2020. MESH1 is a cytosolic NADPH phosphatase that regulates ferroptosis. Nat. Metab. 2(3), 270-277. https://doi.org/10.1038/s42255-020-0181-1.

Dufort-Gervais J, Mongrain V, Brouillette J. 2019. Bidirectional relationships between sleep and amyloid-beta in the hippocampus. Neurobiol. Learn. Mem. 160, 108-117. https://doi.org/10.1016/j.nlm.2018.06.009.

Dufort-Gervais J, Provost C, Charbonneau L, Norris CM, Calon F, Mongrain V, Brouillette J. 2020. Neuroligin-1 is altered in the hippocampus of Alzheimer's disease patients and mouse models, and modulates the toxicity of amyloid-beta oligomers. Sci. Rep. 10, 6956. https://doi.org/10.1038/s41598-020-63255-6.

El Helou J, Bélanger-Nelson E, Freyburger M, Dorsaz S, Curie T, La Spada F, Gaudreault PO, Beaumont É, Pouliot P, Lesage F, Frank MG, Franken P, Mongrain V. 2013. Neuroligin-1 links neuronal activity to sleep-wake regulation. Proc. Natl. Acad. Sci. USA 110, 9974-9979. https://doi.org/10.1073/pnas.1221381110.

Foley J, Blutstein T, Lee S, Erneux C, Halassa MM, Haydon P. 2017. Astrocytic IP3/Ca2+ signaling modulates theta rhythm and REM sleep. Front. Neural Circuits. 11, 3. https://doi.org/10.3389/fncir.2017.00003.

Fraser T, Tayler H, Love S. 2010. Fatty acid composition of frontal, temporal and parietal neocortex in the normal human brain and in Alzheimer's disease. Neurochem. Res. 35, 503-513. https://doi.org/10.1007/s11064-009-0087-5.

Gelinas R, Thompson-Legault J, Bouchard B, Daneault C, Mansour A, Gillis MA, Charron G, Gavino V, Labarthe F, Des Rosiers C. 2011. Prolonged QT interval and lipid alterations beyond beta-oxidation in very long-chain acyl-CoA dehydrogenase null mouse hearts. Am. J. Physiol. Heart Circ. Physiol. 301, H813-H823.

González-Molina LA, Villar-Vesga J, Henao-Restrepo J, Villegas A, Lopera F, Cardona-Gómez GP, Posada-Duque R. 2021. Extracellular vesicles from 3xTg-AD mouse and Alzheimer's disease patient astrocytes impair neuroglial and vascular components. Front. Aging Neurosci. 13, 593927. https://doi.org/10.3389/fnagi.2021.593927.

Goodman LD, Moulton MJ, Lin G, Bellen HJ. 2024. Does glial lipid dysregulation alter sleep in Alzheimer's and Parkinson's disease? Trends Mol. Med. 30, 913-923. https://doi.org/10.1016/j.molmed.2024.04.010.

Gustavsson A, Norton N, Fast T, Frölich L, Georges J, Holzapfel D, Kirabali T, Krolak-Salmon P, Rossini PM, Ferretti MT, Lanman L, Chadha AS, van der Flier WM. 2023. Global estimates on the number of persons across the Alzheimer's disease continuum. Alzheimers Dement. 19, 658-670. https://doi.org/10.1002/alz.12694.

Halassa MM, Florian C, Fellin T, Munoz JR, Lee SY, Abel T, Haydon PG, Frank MG. 2009. Astrocytic modulation of sleep homeostasis and cognitive consequences of sleep loss. Neuron 61, 213-219. https://doi.org/10.1016/j.neuron.2008.11.024.

Hamilton LK, Dufresne M, Joppé SE, Petryszyn S, Aumont A, Calon F, Barnabé-Heider F, Furtos A, Parent M, Chaurand P, Fernandes KJ. 2015. Aberrant lipid metabolism in the forebrain niche suppresses adult neural stem cell proliferation in an animal model of Alzheimer's disease. Cell. Stem. Cell. 17, 397-411. https://doi.org/10.1016/j.stem.2015.08.001.

Hamilton LK, Moquin-Beaudry G, Mangahas CL, Pratesi F, Aubin M, Aumont A, Joppé SE, Légiot A, Vachon A, Plourde M, Mounier C, Tétreault M, Fernandes KJL. 2022. Stearoyl-CoA Desaturase inhibition reverses immune, synaptic and cognitive impairments in an Alzheimer's disease mouse model. Nat. Commun. 13, 2061. https://doi.org/10.1038/s41467-022-29506-y. Erratum in: https://doi.org/10.1038/s41467-023-38295-x.

Haynes PR, Pyfrom ES, Li Y, Stein C, Cuddapah VA, Jacobs JA, Yue Z, Sehgal A. 2024. A neuron-glia lipid metabolic cycle couples daily sleep to mitochondrial homeostasis. Nat. Neurosci. 27(4), 666-678. https://doi.org/10.1038/s41593-023-01568-1.

Hector A, da Costa Caiado MJ, Leduc T, Delignat-Lavaud B, Dufort-Gervais J, Bourguignon C, Lina JM, Fernandes K, Brouillette J, Mongrain V. 2024. Electrocorticographic and astrocytic signatures of stearoyl-CoA desaturase inhibition in the triple transgenic mouse model of Alzheimer's disease. bioRxiv 2024.03.01.582986. https://doi.org/10.1101/2024.03.01.582986.

Hector A, Provost C, Delignat-Lavaud B, Bouamira K, Menaouar CA, Mongrain V, Brouillette J. 2023 Hippocampal injections of soluble amyloid-beta oligomers alter electroencephalographic activity during wake and slow wave sleep in rats. Alzheimers Res. Ther. 15, 174. https://doi.org/10.1186/s13195-023-01316-4.

Heneka MT, Carson MJ, El Khoury J, Landreth GE, Brosseron F, Feinstein DL, Jacobs AH, Wyss-Coray T, Vitorica J, Ransohoff RM, Herrup K, Frautschy SA, Finsen B, Brown GC, Verkhratsky A, Yamanaka K, Koistinaho J, Latz E, Halle A, Petzold GC, Town T, Morgan D, Shinohara ML, Perry VH, Holmes C, Bazan NG, Brooks DJ, Hunot S, Joseph B, Deigendesch N, Garaschuk O, Boddeke E, Dinarello CA, Breitner JC, Cole GM, Golenbock DT, Kummer MP. 2015. Neuroinflammation in Alzheimer's disease. Lancet Neurol. 14, 388-405. https://doi.org/10.1016/S1474-4422(15)70016-5.

Hirata-Fukae C, Li HF, Hoe HS, Gray AJ, Minami SS, Hamada K, Niikura T, Hua F, Tsukagoshi-Nagai H, Horikoshi-Sakuraba Y, Mughal M, Rebeck GW, LaFerla FM, Mattson MP, Iwata N, Saido TC, Klein WL, Duff KE, Aisen PS, Matsuoka Y. 2008. Females exhibit more extensive amyloid, but not tau, pathology in an Alzheimer transgenic model. Brain Res. 1216, 92-103. https://doi.org/10.1016/j.brainres.2008.03.079.

Hook M, Xu F, Terenina E, Zhao W, Starlard-Davenport A, Mormede P, Jones BC, Mulligan MK, Lu L. 2019. Exploring the involvement of Tac2 in the mouse hippocampal stress response through gene networking. Gene. 696, 176-185. https://doi.org/10.1016/j.gene.2019.02.013.

Ioannou MS, Jackson J, Sheu SH, Chang CL, Weigel AV, Liu H, Pasolli HA, Xu CS, Pang S, Matthies D, Hess HF, Lippincott-Schwartz J, Liu Z. 2019. Neuron-astrocyte metabolic coupling protects against activity-induced fatty acid toxicity. Cell. 177, 1522-1535.e14. doi: https://doi.org/10.1016/j.cell.2019.04.001.

Jiang WR, Wu W, Yang LJ, Yang W, Tian Q, Yao ZH. 2023. Alteration of cognitive function in aging and Alzheimer's disease mice is related to dysfunction of the neuroimmune system. J. Alzheimers. Dis. 94(2), 815-839. https://doi.org/10.3233/JAD-230292.

Kaizuka T, Hirouchi T, Saneyoshi T, Shirafuji T, Collins MO, Grant SGN, Hayashi Y, Takumi T. 2024. FAM81A is a postsynaptic protein that regulates the condensation of postsynaptic proteins via liquid-liquid phase separation. PLoS Biol. 22(3), e3002006. https://doi.org/10.1371/journal.pbio.3002006.

Kent BA, Feldman HH, Nygaard HB. 2021. Sleep and its regulation: An emerging pathogenic and treatment frontier in Alzheimer's disease. Prog. Neurobiol. 197, 101902. https://doi.org/10.1016/j.pneurobio.2020.101902.

Kent BA, Michalik M, Marchant EG, Yau KW, Feldman HH, Mistlberger RE, Nygaard HB. 2019. Delayed daily activity and reduced NREM slow-wave power in the APPswe/PS1dE9 mouse model of Alzheimer's disease. Neurobiol. Aging. 78, 74-86. https://doi.org/10.1016/j.neurobiolaging.2019.01.010.

Kent BA, Strittmatter SM, Nygaard HB. 2018. Sleep and EEG power spectral analysis in three transgenic mouse models of Alzheimer's disease: APP/PS1, 3xTgAD, and Tg2576. J. Alzheimers Dis. 64, 1325-1336. http://dx.doi.org/10.3233/JAD-180260.

Kim GS, Harmon E, Gutierrez M, Stephenson J, Chauhan A, Banerjee A, Wise Z, Doan A, Wu T, Lee J, Jung JE, McCullough L, Wythe J, Marrelli S. 2023. Single-cell analysis identifies Ifi27l2a as a novel gene regulator of microglial inflammation in the context of aging and stroke. Res. Sq. [Preprint]. rs.3.rs-2557290. https://doi.org/10.21203/rs.3.rs-2557290/v1.

Klein M, Lohr C, Droste D. 2020. Age-dependent heterogeneity of murine olfactory bulb astrocytes. Front. Aging Neurosci. 12, 172. https://doi.org/10.3389/fnagi.2020.00172.

Kosel F, Pelley JMS, Franklin TB. 2020. Behavioural and psychological symptoms of dementia in mouse models of Alzheimer's disease-related pathology. Neurosci. Biobehav. Rev. 112, 634-647. https://doi.org/10.1016/j.neubiorev.2020.02.012.

Kurkinen M. 2023. Lecanemab (Leqembi) is not the right drug for patients with Alzheimer's disease. Adv. Clin. Exp. Med. 32, 943-947. https://doi.org/10.17219/acem/171379.

Landry O, François A, Oye Mintsa Mi-Mba MF, Traversy MT, Tremblay C, Emond V, Bennett DA, Gylys KH, Buxbaum JD, Calon F. 2023. Postsynaptic protein Shank3a deficiency synergizes with Alzheimer's disease neuropathology to impair cognitive performance in the 3xTg-AD murine model. J. Neurosci. 43(26), 4941-4954. doi: 10.1523/JNEUROSCI.1945-22.2023.

Lau ZJ, Pham T, Chen SHA, Makowski D. 2022. Brain entropy, fractal dimensions and predictability: A review of complexity measures for EEG in healthy and neuropsychiatric populations. Eur. J. Neurosci. 56, 5047-5069. https://doi.org/10.1111/ejn.15800.

Lautenschlager NT, Cupples LA, Rao VS, Auerbach SA, Becker R, Burke J, Chui H, Duara R, Foley EJ, Glatt SL, Green RC, Jones R, Karlinsky H, Kukull WA, Kurz A, Larson EB, Martelli K, Sadovnick AD, Volicer L, Waring SC, Growdon JH, Farrer LA. 1996. Risk of dementia among relatives of Alzheimer’s disease patients in the MIRAGE study: what is in store for the oldest old? Neurology. 46, 641–650. https://doi.org/10.1212/WNL.46.3.641.

Lee JA, Hall B, Allsop J, Alqarni R, Allen SP. 2021. Lipid metabolism in astrocytic structure and function. Semin. Cell Dev. Biol. 112, 123-136. https://doi.org/10.1016/j.semcdb.2020.07.017.

Lee YF, Russ AN, Zhao Q, Perle SJ, Maci M, Miller MR, Hou SS, Algamal M, Zhao Z, Li H, Gelwan N, Liu Z, Gomperts SN, Araque A, Galea E, Bacskai BJ, Kastanenka KV. 2023. Optogenetic targeting of astrocytes restores slow brain rhythm function and slows Alzheimer's disease pathology. Sci. Rep. 13, 13075.

Lin CC, Ding CC, Sun T, Wu J, Chen KY, Zhou P, Chi JT. 2021. The regulation of ferroptosis by MESH1 through the activation of the integrative stress response. Cell Death Dis. 12(8), 727. https://doi.org/10.1038/s41419-021-04018-7.

Lina JM, O'Callaghan EK, Mongrain V. 2019. Scale-Free Dynamics of the mouse wakefulness and sleep electroencephalogram quantified using Wavelet-Leaders. Clocks Sleep. 1, 50-64. https://doi.org/10.3390/clockssleep1010006.

Liu S, Li H, Shen Y, Zhu W, Wang Y, Wang J, Zhang N, Li C, Xie L, Wu Q. 2023. Moxibustion improves hypothalamus Aqp4 polarization in APP/PS1 mice: Evidence from spatial transcriptomics. Front. Aging Neurosci. 15, 1069155. https://doi.org/10.3389/fnagi.2023.1069155.

Lowery RL, Cealie MY, Lamantia CE, Mendes MS, Drew PD, Majewska AK. 2021. Microglia and astrocytes show limited, acute alterations in morphology and protein expression following a single developmental alcohol exposure. J. Neurosci. Res. 99, 2008-2025. https://doi.org/10.1002/jnr.24808.

Ma C, Li B, Silverman D, Ding X, Li A, Xiao C, Huang G, Worden K, Muroy S, Chen W, Xu Z, Tso CF, Huang Y, Zhang Y, Luo Q, Saijo K, Dan Y. 2024. Microglia regulate sleep through calcium-dependent modulation of norepinephrine transmission. Nat. Neurosci. 27, 249-258. https://doi.org/10.1038/s41593-023-01548-5.

Ma Q, Ning X, Wang J, Li J. 2005. Sleep-stage characterization by nonlinear EEG analysis using Wavelet-based multifractal formalism. Conf. Proc. IEEE Eng. Med. Biol. Soc. 2005, 4526-4529. https://doi.org/10.1109/IEMBS.2005.1615475.

Madsen S, Delgado AC, Cadilhac C, Maillard V, Battiston F, Igelbüscher CM, De Neck S, Magrinelli E, Jabaudon D, Telley L, Doetsch F, Knobloch M. 2024. A fluorescent perilipin 2 knock-in mouse model reveals a high abundance of lipid droplets in the developing and adult brain. Nat. Commun. 15, 5489. https://doi.org/10.1038/s41467-024-49449-w.

Mi Y, Qi G, Vitali F, Shang Y, Raikes AC, Wang T, Jin Y, Brinton RD, Gu H, Yin F. 2023. Loss of fatty acid degradation by astrocytic mitochondria triggers neuroinflammation and neurodegeneration. Nat. Metab. 5, 445-465. https://doi.org/10.1038/s42255-023-00756-4.

Miyoshi E, Morabito S, Henningfield CM, Das S, Rahimzadeh N, Shabestari SK, Michael N, Emerson N, Reese F, Shi Z, Cao Z, Srinivasan SS, Scarfone VM, Arreola MA, Lu J, Wright S, Silva J, Leavy K, Lott IT, Doran E, Yong WH, Shahin S, Perez-Rosendahl M; Alzheimer's Biomarkers Consortium–Down Syndrome (ABC–DS); Head E, Green KN, Swarup V. 2024. Spatial and single-nucleus transcriptomic analysis of genetic and sporadic forms of Alzheimer's disease. Nat. Genet. 56, 2704-2717. https://doi.org/10.1038/s41588-024-01961-x.

Murphy-Royal C, Ching S, Papouin T. 2023. A conceptual framework for astrocyte function. Nat. Neurosci. 26, 1848-1856. https://doi.org/10.1038/s41593-023-01448-8.

Murphy-Royal C, Johnston AD, Boyce AKJ, Diaz-Castro B, Institoris A, Peringod G, Zhang O, Stout RF, Spray DC, Thompson RJ, Khakh BS, Bains JS, Gordon GR. 2020. Stress gates an astrocytic energy reservoir to impair synaptic plasticity. Nat. Commun. 11, 2014. https://doi.org/10.1038/s41467-020-15778-9.

Nikhil K, Viccaro K, Shah K. 2019. Multifaceted regulation of ALDH1A1 by Cdk5 in Alzheimer's disease pathogenesis. Mol. Neurobiol. 56(2), 1366-1390. https://doi.org/10.1007/s12035-018-1114-9.

Ochi S, Iga JI, Funahashi Y, Yoshino Y, Yamazaki K, Kumon H, Mori H, Ozaki Y, Mori T, Ueno SI. 2020. Identifying blood transcriptome biomarkers of Alzheimer's disease using transgenic mice. Mol. Neurobiol. 57, 4941-4951. https://doi.org/10.1007/s12035-020-02058-2.

Oddo S, Caccamo A, Shepherd JD, Murphy MP, Golde TE, Kayed R, Metherate R, Mattson MP, Akbari Y, LaFerla FM. 2003. Triple-transgenic model of Alzheimer's disease with plaques and tangles: intracellular Abeta and synaptic dysfunction. Neuron. 39, 409-421. https://doi.org/10.1016/S0896-6273(03)00434-3.

Olabarria M, Noristani HN, Verkhratsky A, Rodríguez JJ. 2010. Concomitant astroglial atrophy and astrogliosis in a triple transgenic animal model of Alzheimer's disease. Glia 58, 831-838. https://doi.org/10.1002/glia.20967.

Olabarria M, Noristani HN, Verkhratsky A, Rodríguez JJ. 2011. Age-dependent decrease in glutamine synthetase expression in the hippocampal astroglia of the triple transgenic Alzheimer's disease mouse model: mechanism for deficient glutamatergic transmission? Mol. Neurodegener. 6, 55. https://doi.org/10.1186/1750-1326-6-55.

Petrelli F, Rey A, Panfilova D, Madsen S, Héritier N, Knobloch M. 2024, An optimized method to visualize lipid droplets in brain tissue demonstrates their substantial accumulation in aged brains. bioRxiv 2024.06.12.598519. https://doi.org/10.1101/2024.06.12.598519.

Rodríguez JJ, Yeh CY, Terzieva S, Olabarria M, Kulijewicz-Nawrot M, Verkhratsky A. 2014. Complex and region-specific changes in astroglial markers in the aging brain. Neurobiol. Aging 35, 15-23. https://doi.org/10.1016/j.neurobiolaging.2013.07.002.

Saber M, Murphy SM, Cho Y, Lifshitz J, Rowe RK. 2021. Experimental diffuse brain injury and a model of Alzheimer's disease exhibit disease-specific changes in sleep and incongruous peripheral inflammation. J. Neurosci. Res. 99, 1136-1160. https://doi.org/10.1002/jnr.24771.

Shi L, Chen SJ, Ma MY, Bao YP, Han Y, Wang YM, Shi J, Vitiello MV, Lu L. 2018. Sleep disturbances increase the risk of dementia: A systematic review and meta-analysis. Sleep Med. Rev. 40, 4-16. https://doi.org/10.1016/j.smrv.2017.06.010.

Skuladottir GV, Nilsson EK, Mwinyi J, Schiöth HB. 2016. One-night sleep deprivation induces changes in the DNA methylation and serum activity indices of stearoyl-CoA desaturase in young healthy men. Lipids Health Dis. 15, 137. https://doi.org/10.1186/s12944-016-0309-1.

Smolič T, Tavčar P, Horvat A, Černe U, Halužan Vasle A, Tratnjek L, Kreft ME, Scholz N, Matis M, Petan T, Zorec R, Vardjan N. 2021. Astrocytes in stress accumulate lipid droplets. Glia 69, 1540-1562. https://doi.org/10.1002/glia.23978.

Sterniczuk R, Dyck RH, Laferla FM, Antle MC. 2010. Characterization of the 3xTg-AD mouse model of Alzheimer's disease: part 1. Circadian changes. Brain Res. 1348, 139-148. https://doi.org/10.1016/j.brainres.2010.05.013.

Sun M, Chen X, Yang Z. 2022. Single cell mass spectrometry studies reveal metabolomic features and potential mechanisms of drug-resistant cancer cell lines. Anal. Chim. Acta. 1206, 339761. https://doi.org/10.1016/j.aca.2022.339761.

Tavares, G., Martins, M., Correia, J.S., Sardinha, V.M., Guerra-Gomes, S., das Neves, S.P., Marques, F., Sousa, N., Oliveira, J.F. 2017. Employing an open-source tool to assess astrocyte tridimensional structure. Brain Struct. Funct. 222, 1989–1999. https://doi.org/10.1007/s00429-016-1316-8.

Teerlink CC, Miller JB, Vance EL, Staley LA, Stevens J, Tavana JP, Cloward ME, Page ML, Dayton L; Alzheimer's Disease Genetics Consortium; Cannon-Albright LA, Kauwe JSK. 2022. Analysis of high-risk pedigrees identifies 11 candidate variants for Alzheimer's disease. Alzheimers Dement. 18(2), 307-317. https://doi.org/10.1002/alz.12397.

Thompson Legault J, Strittmatter L, Tardif J, Sharma R, Tremblay-Vaillancourt V, Aubut C, Boucher G, Clish CB, Cyr D, Daneault C, Waters PJ; LSFC Consortium; Vachon L, Morin C, Laprise C, Rioux JD, Mootha VK, Des Rosiers C. 2015. A metabolic signature of mitochondrial dysfunction revealed through a monogenic form of Leigh syndrome. Cell Rep. 13, 981-989. https://doi.org/10.1016/j.celrep.2015.09.054.

Turcot V, Brunet J, Daneault C, Tardif JC, Des Rosiers C, Lettre G. 2015. Validation of fatty acid intakes estimated by a food frequency questionnaire using erythrocyte fatty acid profiling in the Montreal Heart Institute Biobank. J. Hum. Nutr. Diet. 28, 646–658.

Ugolini F, Lana D, Nardiello P, Nosi D, Pantano D, Casamenti F, Giovannini MG. 2018. Different patterns of neurodegeneration and glia activation in CA1 and CA3 hippocampal regions of TgCRND8 mice. Front. Aging Neurosci. 10, 372. https://doi.org/10.3389/fnagi.2018.00372.

Vassalli A, Franken P. 2017. Hypocretin (orexin) is critical in sustaining theta/gamma-rich waking behaviors that drive sleep need. Proc. Natl. Acad. Sci. USA. 114, E5464-E5473. https://doi.org/10.1073/pnas.1700983114.

Wan L, Ai JQ, Yang C, Jiang J, Zhang QL, Luo ZH, Huang RJ, Tu T, Pan A, Tu E, Manavis J, Xiao B, Yan XX. 2021. Expression of the excitatory postsynaptic scaffolding protein, Shank3, in human brain: effect of age and Alzheimer's disease. Front. Aging Neurosci. 13, 717263. https://doi.org/10.3389/fnagi.2021.717263.

Wang C, Acosta D, McNutt M, Bian J, Ma A, Fu H, Ma Q. 2024. A single-cell and spatial RNA-seq database for Alzheimer's disease (ssREAD). Nat. Commun. 15, 4710. https://doi.org/10.1038/s41467-024-49133-z.

Wang C, Holtzman DM. 2020. Bidirectional relationship between sleep and Alzheimer's disease: role of amyloid, tau, and other factors. Neuropsychopharmacology 45, 104-120. https://doi.org/10.1038/s41386-019-0478-5.

Weiss B, Clemens Z, Bódizs R, Vágó Z, Halász P. 2009. Spatio-temporal analysis of monofractal and multifractal properties of the human sleep EEG. J. Neurosci. Methods 185, 116-124. https://doi.org/10.1016/j.jneumeth.2009.07.027.

Wendt H, Roux SG, Abry P, Jaffard S. 2008. Wavelet-leaders and bootstrap for multifractal analysis of images. Signal Process. 89, 1100–1114. https://doi.org/10.1016/j.sigpro.2008.12.015.

Whiley L, Sen A, Heaton J, Proitsi P, García-Gómez D, Leung R, Smith N, Thambisetty M, Kloszewska I, Mecocci P, Soininen H, Tsolaki M, Vellas B, Lovestone S, Legido-Quigley C; AddNeuroMed Consortium. 2014. Evidence of altered phosphatidylcholine metabolism in Alzheimer's disease. Neurobiol. Aging. 35, 271-278. https://doi.org/10.1016/j.neurobiolaging.2013.08.001.

Widjaya MA, Liu CH, Lee SD, Cheng WC. 2023. Transcriptomics meta-analysis reveals phagosome and innate immune system dysfunction as potential mechanisms in the cortex of Alzheimer's disease mouse strains. J. Mol. Neurosci. 73(9-10), 773-786. https://doi.org/10.1007/s12031-023-02152-9.

Wu R, Tripathy S, Menon V, Yu L, Buchman AS, Bennett DA, De Jager PL, Lim ASP. 2023. Fragmentation of rest periods, astrocyte activation, and cognitive decline in older adults with and without Alzheimer's disease. Alzheimers Dement. 19, 1888-1900. https://doi.org/10.1002/alz.12817.

Yeh CY, Vadhwana B, Verkhratsky A, Rodríguez JJ. 2011. Early astrocytic atrophy in the entorhinal cortex of a triple transgenic animal model of Alzheimer's disease. ASN Neuro. 3, 271-279. https://doi.org/10.1042/AN20110025.

Zhang H, Huang Y, Wang W. 2025. Aβ oligomers promote lipid droplet accumulation and inflammatory responses in astrocytes but not neurons. Brain Res. Bull. 231, 111556. https://doi.org/10.1016/j.brainresbull.2025.111556.

Zhang Y, Ren R, Yang L, Zhang H, Shi Y, Okhravi HR, Vitiello MV, Sanford LD, Tang X. 2022. Sleep in Alzheimer's disease: a systematic review and meta-analysis of polysomnographic findings. Transl. Psychiatry. 12, 136. https://doi.org/10.1038/s41398-022-01897-y.

TABLE

Table 1: Summary of selected key findings related to wake/sleep, LD, astrocytic and transcriptomic variables compared between 3xTg-AD and WT mice treated with vehicle (veh) or SCDi.

		3xTg vs. WT (veh)	3xTg SCDi vs. veh	WT SCDi vs. veh
Time spent (24 hours)	wake	↓	—	—
	SWS	↑	—	—
	PS	—	—	—
Absolute power (bipolar; 24 hours)	wake	↓ SWA, Theta, Alpha, Sigma, Beta	—	—
	SWS	↓ SWA, Theta, Alpha, Sigma, Beta	—	—
	PS	↓ Sigma, Beta, Gamma	—	—
Relative power (bipolar; 24 hours)	wake	↑ SWA ↓ Theta, Alpha	↑ Beta[#], Gamma	↓ Beta[#], Gamma[#]
	SWS	↑ Gamma ↓ Theta, Sigma	—	—
	PS	↑ SWA, Alpha	↑ Sigma, Beta, Gamma[#]	↓ Beta[+], Gamma[+]
Hm (bipolar; 24 hours)	wake	↓	—	—
	SWS	↓	—	—
	PS	—	—	—
D (bipolar; 24 hours)	wake	↑	—	—
	SWS	—	—	—
	PS	↓	—	↓
LDs	CA1	↑	↓	—
	CA3	↓	↑	—
GFAP+ cells	CA1	↑	↓	—
	CA3	↑	—	—
	DG	—	—	—
ALDH1L1+ cells	LH	↑	—	—
	Thalamus	↑	—	—
ALDH1L1 puncta on GFAP+ cells	CA1	↓	—	—
Bulk transcriptome		↑ 3991 DEGs ↓ 1653 DEGs	↑ 432 DEGs ↓ 172 DEGs	↑ 993 DEGs ↓ 1006 DEGs

↑: higher or increased; ↓: lower or decreased; —: no significant change; DEG: differentially expressed genes; LD: lipid droplet; LH: lateral hypothalamus; SWA: slow wave activity; SWS: slow wave sleep; PS: paradoxical sleep; [#]: $p < 0.05$ only versus other genotype with treatment; [+]: $p < 0.05$ mainly for motor and/or visual cortex.

FIGURE LEGENDS

Fig. 1. Wake/sleep architecture variables in 3xTg-AD and WT mice treated with SCDi or vehicle.

(A) Time spent in wakefulness, SWS and PS during the full 24-hour recording (WT + veh n = 12 mice, WT + SCDi n = 12 mice, 3xTg + veh n = 11 mice, and 3xTg + SCDi n = 10 mice; also in all other panels). ***: $p < 0.001$ between genotypes.

(B) Time spent in wakefulness, SWS and PS during the 12-hour light and the 12-hour dark periods. Grey backgrounds indicate the 12-hour dark period (also in panel C). *: $p < 0.05$ and **: $p \leq 0.01$ between indicated genotypes (also in panels C and D).

(C) 24-hour distribution of time spent in wakefulness, SWS and PS.

(D) Number of individual bouts of different durations for wakefulness, SWS and PS, and total number of bouts of each state (tot). #: $p < 0.05$ between SCDi and vehicle.

Fig. 2. ECoG activity of the bipolar signal during the three vigilance states in 3xTg-AD and WT mice treated with SCDi or vehicle.

(A) Mean 24-h power spectra (absolute power) for wake (top), SWS (middle) and PS (bottom). (WT + veh n = 11 mice, WT + SCDi n = 11 mice, 3xTg + veh n = 11 mice, and 3xTg + SCDi n = 10 mice) Black dots on top of graphing areas indicate 0.25 Hz-bins with significant differences between genotypes (wake $F_{1,40} > 4.1$, SWS $F_{1,40} > 4.2$, PS $F_{1,40} > 4.1$, all $p < 0.05$).

(B) Mean 24-h power spectra (relative power) for wake (top), SWS (middle) and PS (bottom). (WT + veh n = 12 mice, WT + SCDi n = 11 mice, 3xTg + veh n = 11 mice, and 3xTg + SCDi n = 10 mice; also for panel C) Black dots on top of graphing area indicate 0.25 Hz-bin with significant differences between genotypes ($F_{1,40} > 4.1$, $p < 0.05$); red dots bins with significant Genotype by Treatment interactions (wake and PS $F_{1,40} > 4.1$, $p < 0.05$); and grey dot the bin with a significant difference between treatments (PS $F_{1,40} = 6.0$, $p < 0.05$).

(C) Mean 12-h light and 12-h dark relative power for six different frequency bands (SWA 0.5-5 Hz, Theta 5-9 Hz, Alpha 9-12 Hz, Sigma 12-16 Hz, Beta 16-30 Hz, Gamma 30-50 Hz) for wake, SWS and PS. Grey backgrounds indicate the 12-hour dark period (also for panels D and E). *: $p < 0.05$, **: $p < 0.01$ and ***: $p < 0.001$ between genotypes (also for panels D and E). Δ: $p < 0.05$ between indicated groups (planned comparisons following significant Genotype by Treatment interaction).

(D) 24-h time course of SWA (first column) and theta activity (second column) for wake (for panels D and E: WT + veh n = 11 or 12 mice, WT + SCDi n = 9 or 11 mice, 3xTg + veh n = 10 or 11 mice, and 3xTg + SCDi n = 10 mice; some mice excluded because of no artifact-free epoch for one or two intervals).

(E) 24-h time course of SWA (first column) and theta activity (second column) for SWS.

Fig. 3. Scale-free activity of the ECoG during wakefulness, SWS and PS in 3xTg-AD and WT mice treated with SCDi or vehicle.

(A) Predominant Hurst exponent (Hm) of the bipolar ECoG signal, computed for the full 24-h recording (left), and per time interval (right) for wake (top), SWS (middle) and PS (bottom). Grey backgrounds indicate the 12-hour dark period (also in panel D). (full 24-h recording WT + veh n = 12 mice, WT + SCDi n = 11 mice, 3xTg + veh n = 10 or 11 mice, and 3xTg + SCDi n = 9 mice [also for panels B, D and E]; for the analyses per interval WT + veh n = 7 to 12 mice, WT + SCDi n = 9 to 11 mice, 3xTg + veh n = 6 or 10 mice, and 3xTg + SCDi n = 8 or 9 mice [also for panel D]; some animals excluded because of no artifact-free epoch for some intervals, in particular for PS, or because of outlier values) *: $p < 0.05$ between genotypes (also for all other panels).

(B) Hm computed for the full 24-h recording during wake (top), SWS (middle) and PS (bottom) for the motor cortex.

(C) Hm computed for the full 24-h recording during the three states for the visual cortex. (WT + veh n = 11 mice, WT + SCDi n = 11 mice, 3xTg + veh n = 10 mice, and 3xTg + SCDi n = 8 mice; also for panel F).

(D) Dispersion (D) of Hurst exponents around Hm for the bipolar ECoG signal, computed for the whole 24-h recording (left), and per time interval (right) for wake (top), SWS (middle) and PS (bottom). Δ: $p < 0.05$ between indicated groups (planned comparisons following significant Genotype by Treatment interaction).

(E) D computed for the full 24-h recording during wake (top), SWS (middle) and PS (bottom) for the motor cortex.

(F) D computed for the full 24-h recording during the three states for the visual cortex. Δ: $p < 0.05$ between indicated groups (planned comparisons following significant Genotype by Treatment interaction).

Fig. 4. Whole-hemisphere levels of fatty acids and hippocampal quantification of LDs in 3xTg-AD and WT mice treated with SCDi or vehicle.

(A) Selected fatty acids bound to triglycerides and phospholipids plus free fatty acids (FFA) shown together with the ratio of palmitoleic to palmitic acids and saturated fatty acids (SFAs) expressed at low level for the four experimental groups (WT + veh n = 7 mice, WT + SCDi n = 7 mice, 3xTg + veh n = 7 mice, and 3xTg + SCDi n = 6 mice). *: $p < 0.05$ and **: $p < 0.01$ between genotypes, and

Δ: $p < 0.05$ between indicated groups (planned comparisons following significant Genotype by Treatment interaction).

(B) Representative images of LDs and clusters of LDs (red) shown for each of the experimental group separately for CA1 and CA3 together with NucBlue nuclear staining (turquoise green). Scale bar = 20 μm (same for all panels); full ROIs presented in Fig. S5 and S6.

(C) The number of LDs and LD clusters per cell and of LDs per cell calculated for the pyramidal layer of the CA1 and CA3 regions of the hippocampus (WT + veh n = 23 ROIs for CA1 and 24 ROIs for CA3 [4 mice], WT + SCDi n = 20 ROIs for both CA1 and CA3 [4 mice], 3xTg + veh n = 30 ROIs for CA1 and CA3 [5 mice], and 3xTg + SCDi n = 28 ROIs for CA1 and 30 ROIs for CA3 [5 mice]). ***: $p < 0.001$ between genotypes, and Δ: $p < 0.05$ and ΔΔΔ: $p < 0.001$ between indicated groups (planned comparisons following significant Genotype by Treatment interaction).

Fig. 5. GFAP-positive cell counts in the hippocampus, ALDH1L1-positive cell counts in the LH and thalamus, GFAP-derived CA1 astrocyte morphology and number of ALDH1L1 puncta per GFAP-positive CA1 astrocyte in 3xTg-AD and WT mice treated with SCDi or vehicle.

(A) Representative images (top) and quantification (bottom) of GFAP-positive astrocytes in CA1 and CA3. The red staining is GFAP, and the blue staining DAPI (also for panels C and F). The quantification was computed using the four regions of interest of each animal as different datapoints (WT + veh n = 6 mice, WT + SCDi n = 6 mice, 3xTg + veh n = 6 mice, and 3xTg + SCDi n = 5 mice; also for all other panels). *: $p < 0.05$ between genotypes (also for panel G), and Δ: $p < 0.05$ between indicated groups (i.e., 3xTg + veh vs. both WT + veh and 3xTg + SCDi; planned comparisons following significant Genotype by Treatment interaction).

(B) Representative images (top) and quantification (bottom) of ALDH1L1-positive astrocytes in the LH and thalamus. The yellow staining is ALDH1L1, and blue staining DAPI (also in panel F). The quantification was computed using the four regions of interest of each animal as different datapoints. **: $p < 0.01$ between 3xTg and WT mice.

(C) Representative images of GFAP-positive astrocytes (left) and corresponding skeletons (right) for one animal of each group.

(D) Length of radius shown for six CA1 astrocytes per animal for the four experimental groups. #: $p < 0.05$ between SCDi and vehicle (main Treatment effect).

(E) Mean length of CA1 astrocytic processes plotted for six astrocytes per animal for the four groups.

(F) Representative image of the puncta-like ALDH1L1 staining of a GFAP-positive astrocyte in CA1 for a 3xTg mice treated with SCDi.

(G) Number of ALDH1L1 puncta per CA1 astrocyte shown for six astrocytes per mouse for each group.

Fig. 6. Brain transcriptome (full brain hemisphere slice/bulk) in 3xTg-AD and WT mice treated with SCDi or vehicle.

(A) Volcano plots showing gene expression changes between experimental groups for four different comparisons (fold change: FC). Red (increase/up) and blue (decrease/down) datapoints indicate differentially expressed genes (DEGs; FDR < 0.05). Grey datapoints indicate transcripts without significant change

(B) Table showing the most relevant KEGG (Kyoto Encyclopedia of Genes and Genomes) pathways associated to DEGs between 3xTg and WT mice treated with vehicle. The number of genes associated with each specific term is indicated by the dot size and the significance of enrichment by the dot color (greyscale).

(C) Violin plots and spatial maps of log2 gene expression shown for 3xTg and WT mice treated with vehicle for *Cx3cl1* (fold change [FC] between 3xTg and WT mice = 1.3), *Thy1* (FC = 2.8), *Arrb1* (FC = 1.7), *Mt-atp8* (FC = 0.7), *Atp6v1g2* (FC = 1.3), *Mt-co3* (FC = 0.8), *Tubb4a* (FC = 1.5), and *Klc2* (FC = 1.6) (representative examples of selected KEGG pathways).

(D) Bar and Venn diagrams illustrating the number of overlapping and non-overlapping DEGs among the four different comparisons. Numbers circled in light blue indicate DEGs between 3xTg and WT mice that are also significantly impacted by SCDi treatment in 3xTg mice.

(E) Violin plots and spatial maps of log2 gene expression shown for the four experimental groups for representative examples of DEGs between 3xTg and WT mice that are also significantly impacted by SCDi treatment in 3xTg mice (from categories circled in light blue in panel D; *Aldh1a1* [FC genotype = 0.7, FC SCDi in mutant = 1.3], *Cox6a2* [FC genotype = 0.7, FC SCDi in mutant = 1.2] and *Shank3* [FC genotype = 2.1, FC SCDi in mutant = 0.6]).

Fig. 7. Modifications in the transcriptome of different brain regions in 3xTg-AD and WT mice treated with SCDi or vehicle.

(A) Tables showing the most relevant molecular functions (MF), biological processes (BP), and KEGG (Kyoto Encyclopedia of Genes and Genomes) pathways associated to DEGs between 3xTg and WT mice treated with vehicle for the cerebral cortex, hippocampus and thalamus. The number of genes associated with each specific term is indicated by the dot size and the significance of enrichment by the dot color (greyscale).

(B) Violin plots and spatial maps of log2 gene expression shown for 3xTg and WT mice treated with vehicle for *Lamc2* (fold change [FC] between 3xTg and WT cerebral cortex = 1.9), *Tnnc1* (FC cerebral cortex = 2.3), *Gfap* (FC hippocampus = 4.3), *Parp12* (FC hippocampus = 3.5), *C1qa* (FC

hippocampus = 2.3), *Ighm* (FC cerebral cortex = 2.3, FC hippocampus = 4.9), *Syn1*, *Arrb1*, *Cacng2* and *Gabra3* (all FC thalamus = 1.6 to 3.2), and for *Aldh7a1* (FC thalamus = 2.1, FC hypothalamus = 3.0) and *Rgcc* (FC cortex = 0.6, FC hippocampus = 0.5, FC hypothalamus = 0.3) (representative examples of selected MF, BP or KEGG pathways).

(C) Heatmaps of the Log2 fold change (FC) in expression of the DEGs found for the four brain regions and the two selected comparisons (3xTg vehicle versus WT vehicle and 3xTg SCDi versus 3xTg vehicle). Heatmaps include the DEGs found in at least one of the two comparisons (270 for cortex, 121 for hippocampus, 275 for thalamus, and 171 for hypothalamus). Automated hierarchical clustering showing four different gene clusters is also shown.

(D) Spatial maps of log2 gene expression shown for the four experimental groups for representative examples of DEGs between 3xTg and WT mice that are also significantly impacted by SCDi treatment in 3xTg mice in at least one brain region (*Hddc3* [FC genotype all regions = 0.3 to 0.5, FC SCDi in mutant all regions = 3.2 to 4.6], *Fam81a* [FC genotype thalamus = 3.7, FC SCDi in mutant thalamus = 0.4] and *Pdyn* [FC genotype hypothalamus = 0.5, FC SCDi in mutant hypothalamus = 6.5]).

FIGURE 1

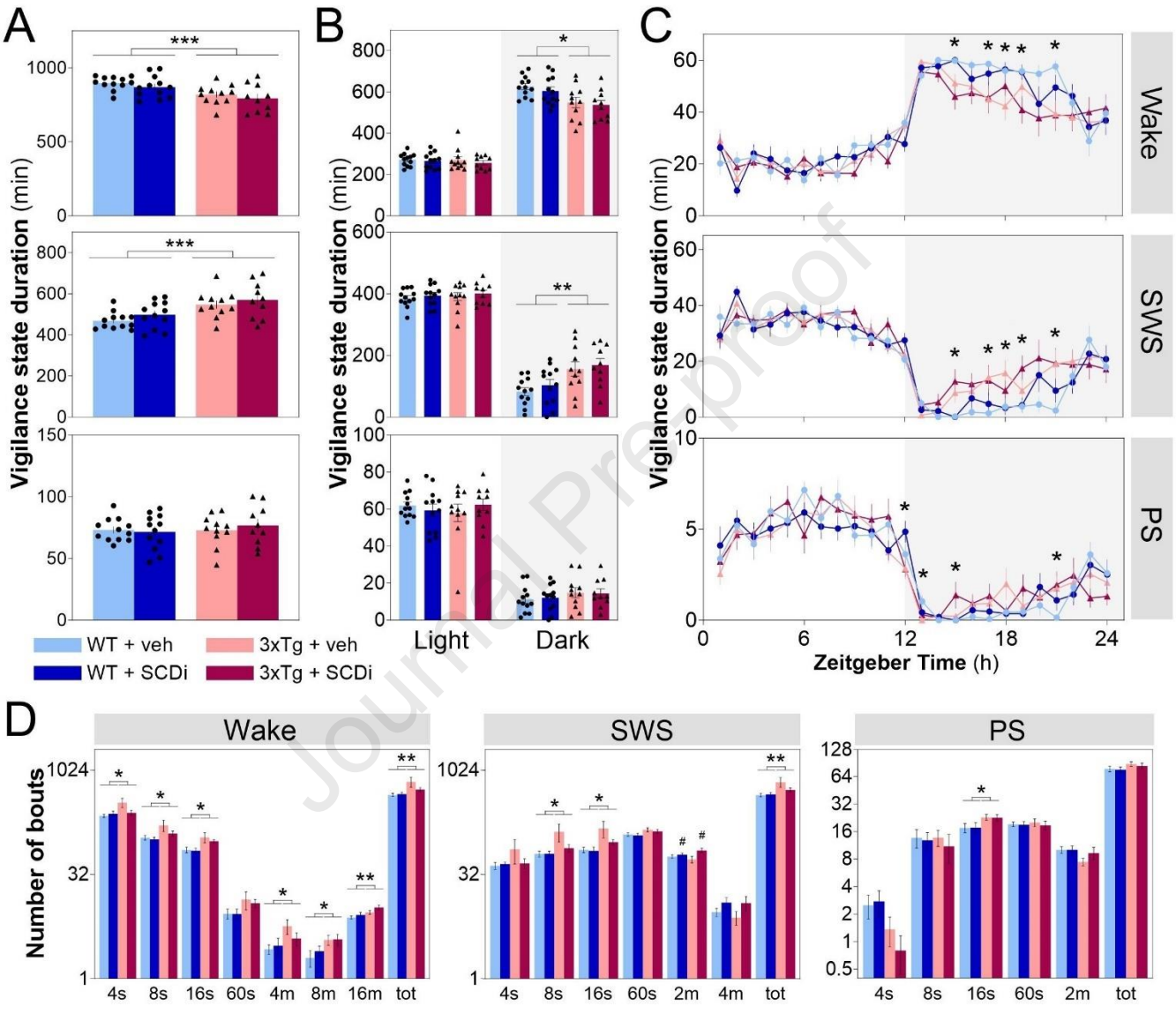

FIGURE 2

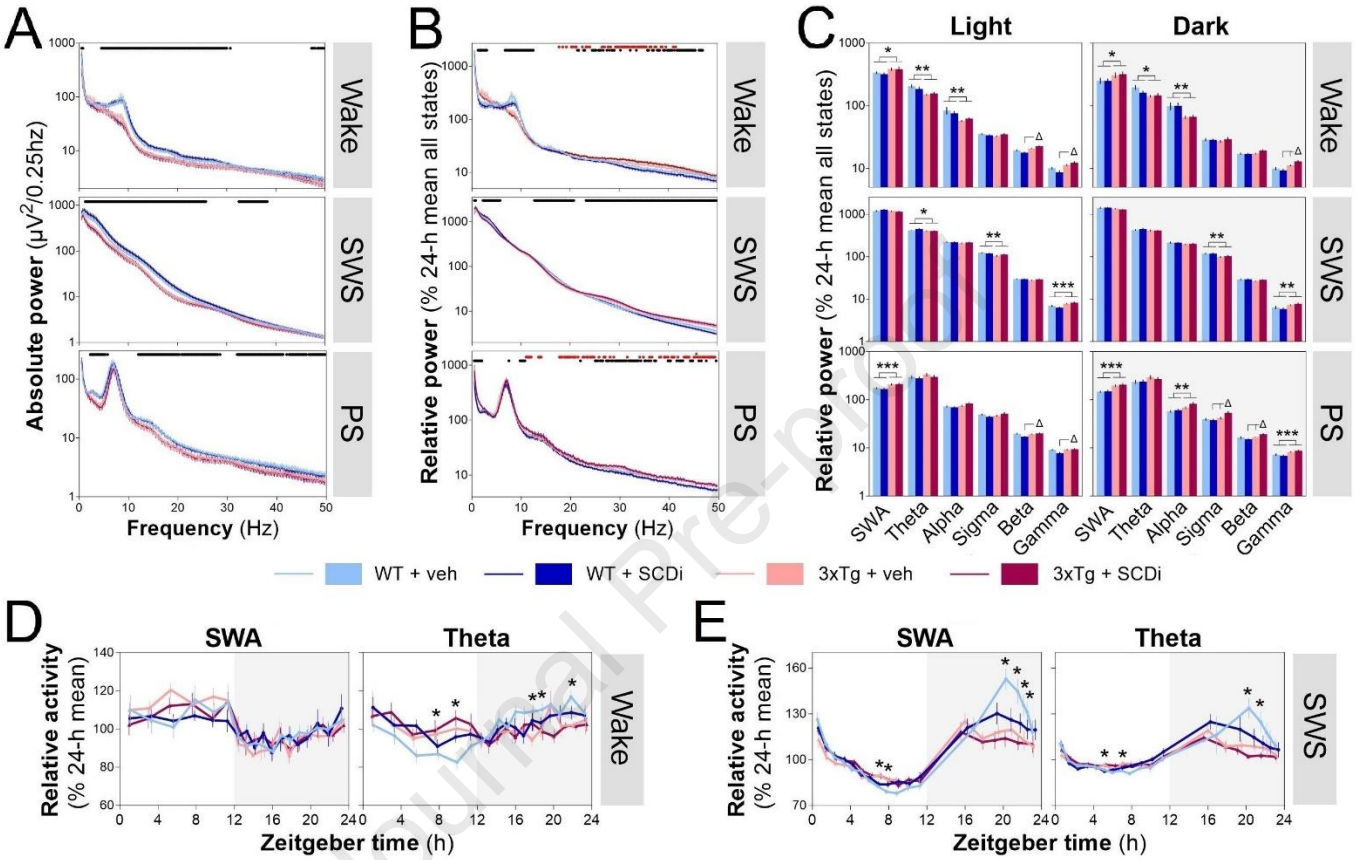

FIGURE 3

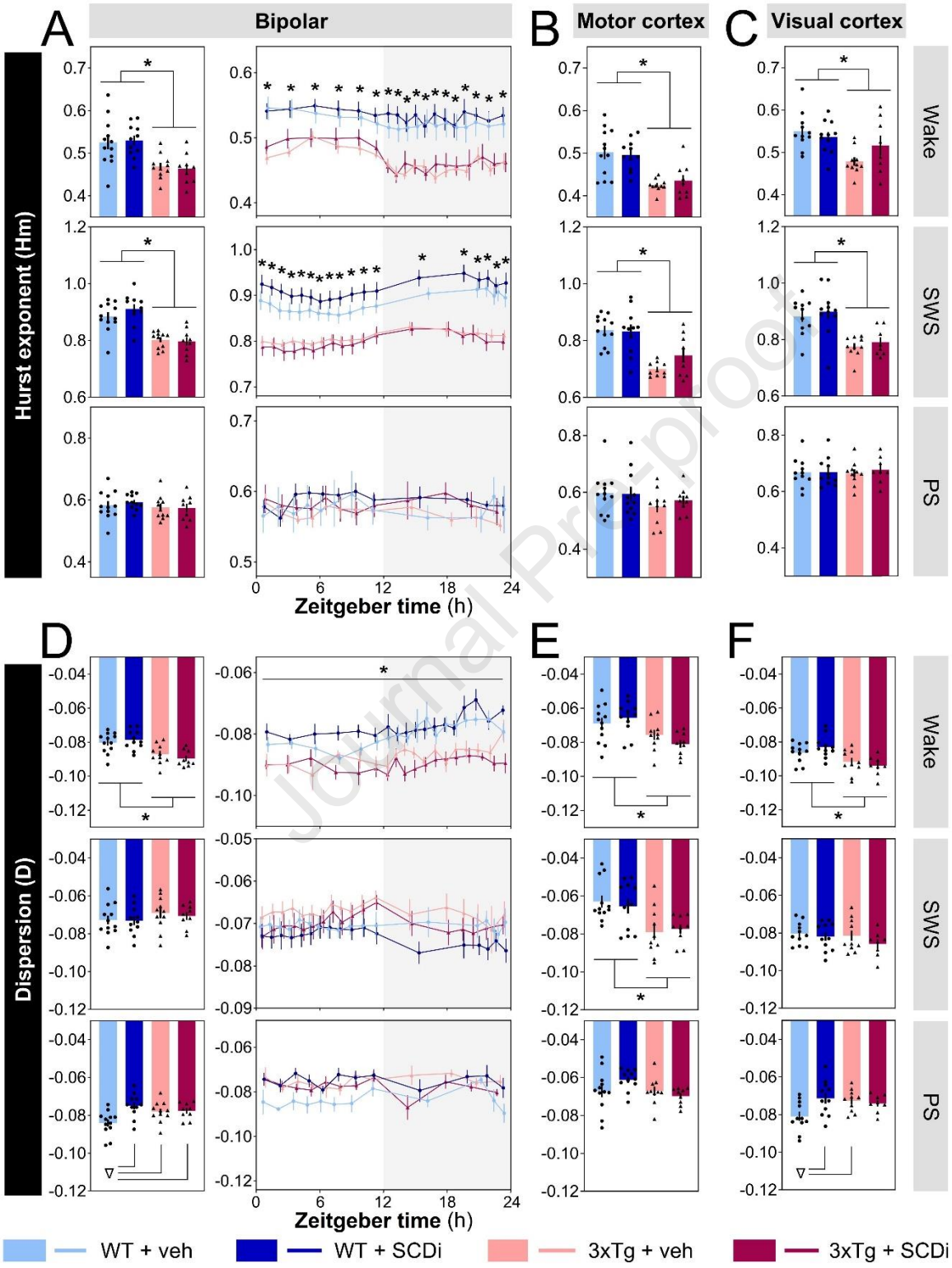

FIGURE 4

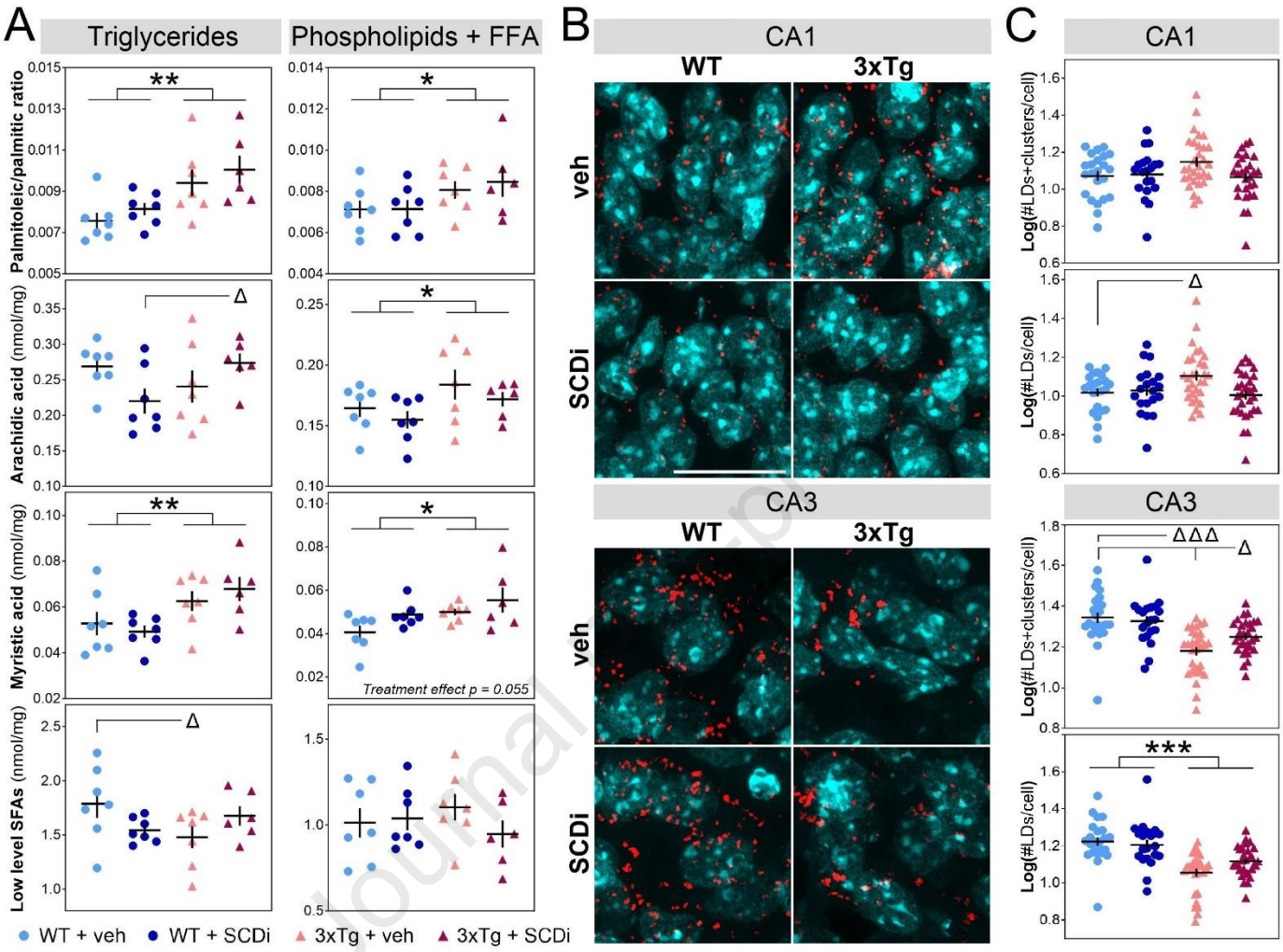
A
Triglycerides
Phospholipids + FFA
Palmitoleic/palmitic ratio
Arachidic acid (nmol/mg)
Myristic acid (nmol/mg)
Low level SFAs (nmol/mg)
Treatment effect p = 0.055
WT + veh
WT + SCDi
3xTg + veh
3xTg + SCDi
B
CA1
WT
3xTg
veh
SCDi
CA3
C
CA1
Log(#LDs+clusters/cell)
Log(#LDs/cell)
CA3

FIGURE 5

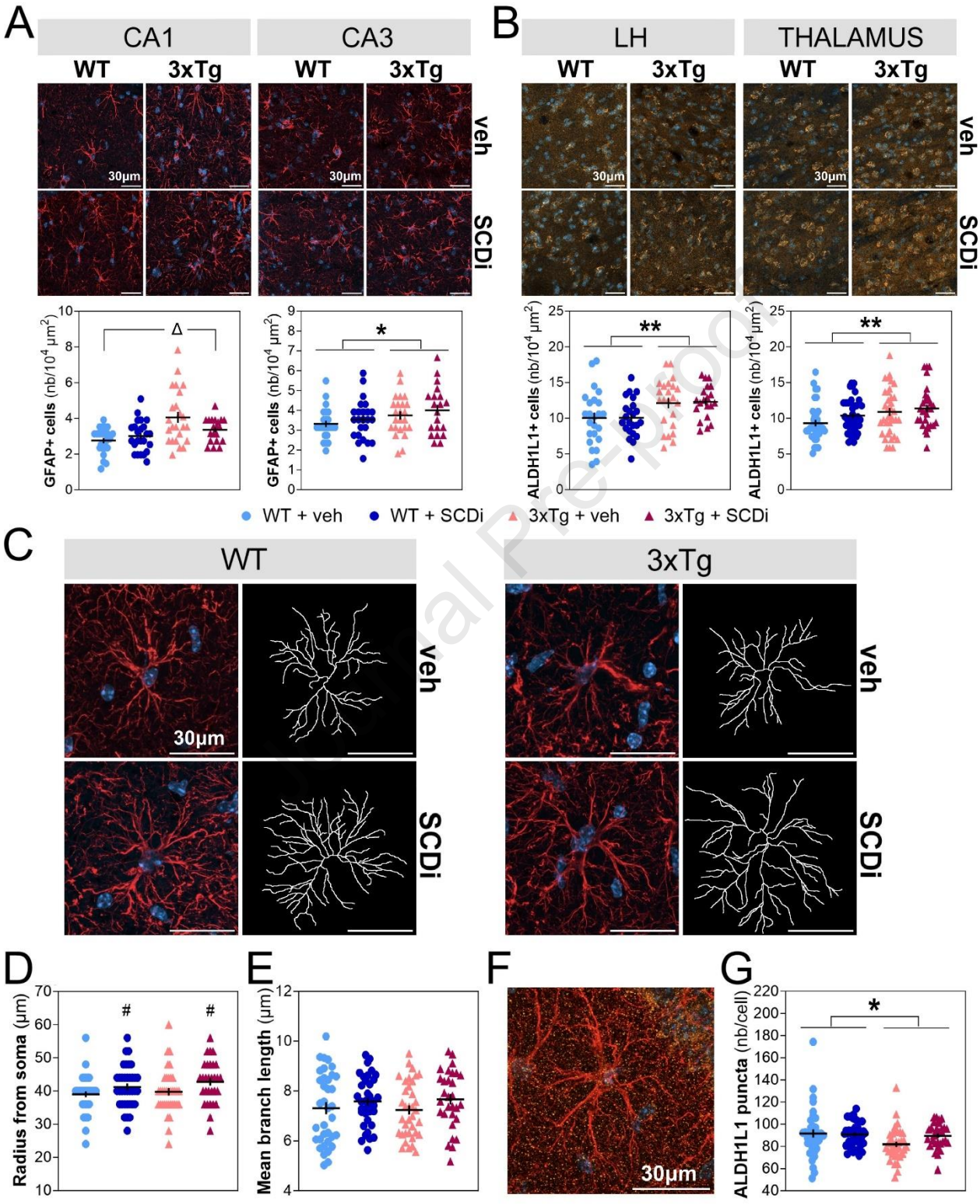
A
CA1
CA3
WT
3xTg
WT
3xTg
veh
SCDi
30µm
GFAP+ cells (nb/10^4 µm^2)
Δ
*
B
LH
THALAMUS
WT
3xTg
WT
3xTg
ALDH1L1+ cells (nb/10^4 µm^2)
**
**
WT + veh
WT + SCDi
3xTg + veh
3xTg + SCDi
C
WT
3xTg
30µm
D
Radius from soma (µm)
#
#
E
Mean branch length (µm)
F
30µm
G
ALDH1L1 puncta (nb/cell)
*

FIGURE 6

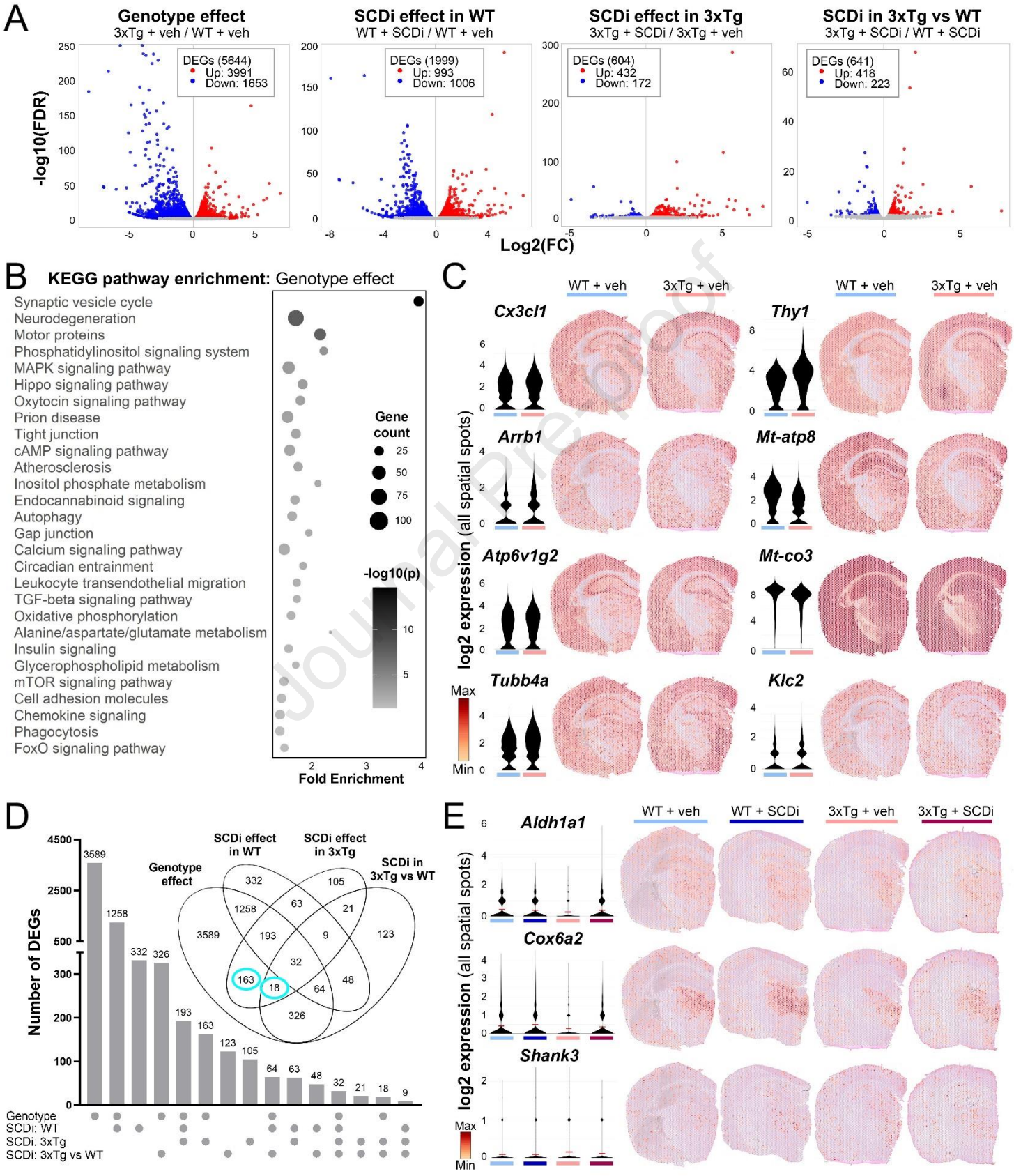
A
Genotype effect
3xTg + veh / WT + veh
DEGs (5644)
Up: 3991
Down: 1653
SCDi effect in WT
WT + SCDi / WT + veh
DEGs (1999)
Up: 993
Down: 1006
SCDi effect in 3xTg
3xTg + SCDi / 3xTg + veh
DEGs (604)
Up: 432
Down: 172
SCDi in 3xTg vs WT
3xTg + SCDi / WT + SCDi
DEGs (641)
Up: 418
Down: 223
-log10(FDR)
Log2(FC)
B
KEGG pathway enrichment: Genotype effect
Synaptic vesicle cycle
Neurodegeneration
Motor proteins
Phosphatidylinositol signaling system
MAPK signaling pathway
Hippo signaling pathway
Oxytocin signaling pathway
Prion disease
Tight junction
cAMP signaling pathway
Atherosclerosis
Inositol phosphate metabolism
Endocannabinoid signaling
Autophagy
Gap junction
Calcium signaling pathway
Circadian entrainment
Leukocyte transendothelial migration
TGF-beta signaling pathway
Oxidative phosphorylation
Alanine/aspartate/glutamate metabolism
Insulin signaling
Glycerophospholipid metabolism
mTOR signaling pathway
Cell adhesion molecules
Chemokine signaling
Phagocytosis
FoxO signaling pathway
Gene count
-log10(p)
Fold Enrichment
C
WT + veh
3xTg + veh
Cx3cl1
Thy1
Arrb1
Mt-atp8
Atp6v1g2
Mt-co3
Tubb4a
Klc2
log2 expression (all spatial spots)
Max
Min
D
Number of DEGs
Genotype effect
SCDi effect in WT
SCDi effect in 3xTg
SCDi in 3xTg vs WT
Genotype
SCDi: WT
SCDi: 3xTg
SCDi: 3xTg vs WT
E
WT + veh
WT + SCDi
3xTg + veh
3xTg + SCDi
Aldh1a1
Cox6a2
Shank3
log2 expression (all spatial spots)
Max
Min

FIGURE 7

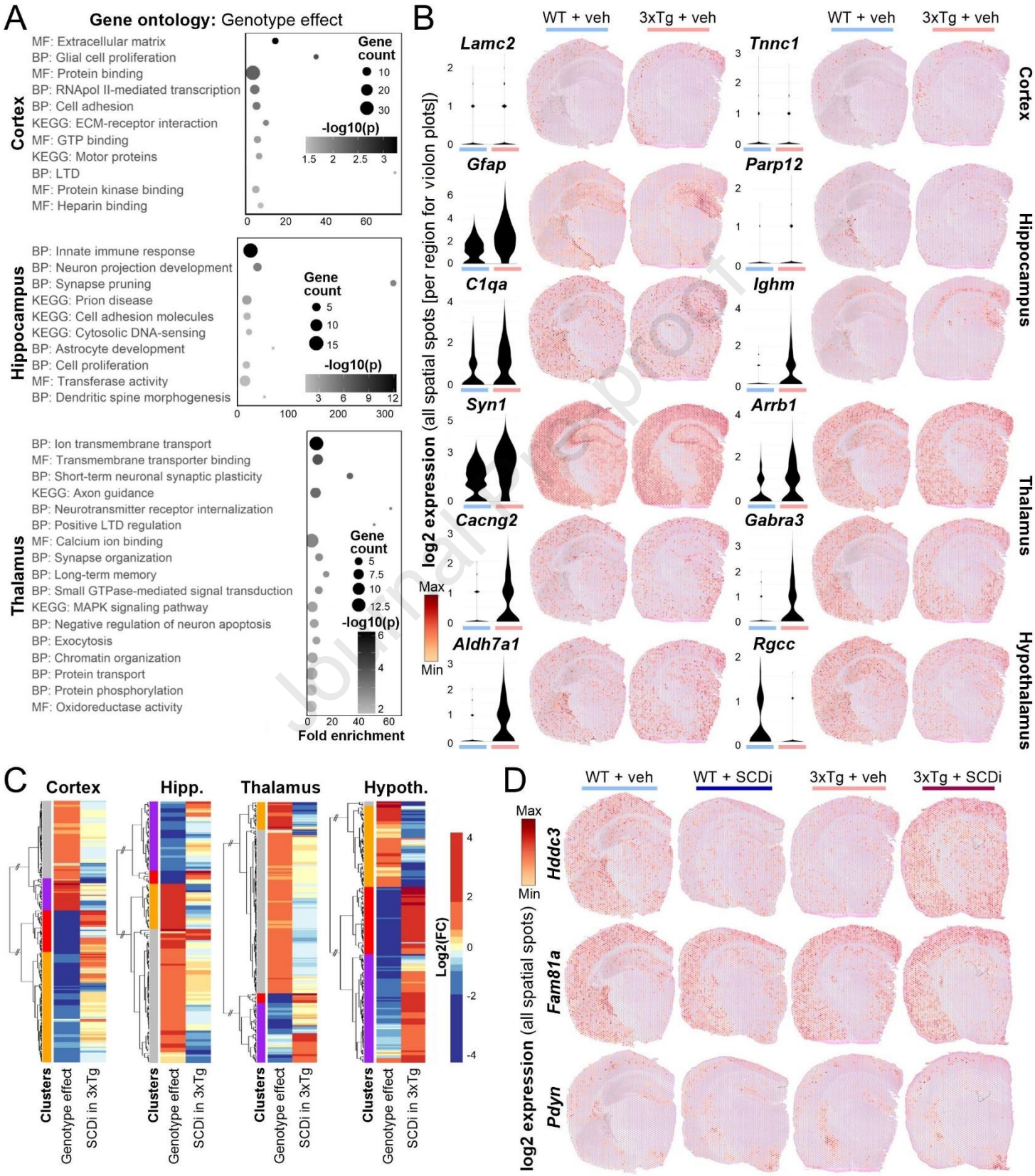
A
Gene ontology: Genotype effect
Cortex
MF: Extracellular matrix
BP: Glial cell proliferation
MF: Protein binding
BP: RNApol II-mediated transcription
BP: Cell adhesion
KEGG: ECM-receptor interaction
MF: GTP binding
KEGG: Motor proteins
BP: LTD
MF: Protein kinase binding
MF: Heparin binding
Hippocampus
BP: Innate immune response
BP: Neuron projection development
BP: Synapse pruning
KEGG: Prion disease
KEGG: Cell adhesion molecules
KEGG: Cytosolic DNA-sensing
BP: Astrocyte development
BP: Cell proliferation
MF: Transferase activity
BP: Dendritic spine morphogenesis
Thalamus
BP: Ion transmembrane transport
MF: Transmembrane transporter binding
BP: Short-term neuronal synaptic plasticity
KEGG: Axon guidance
BP: Neurotransmitter receptor internalization
BP: Positive LTD regulation
MF: Calcium ion binding
BP: Synapse organization
BP: Long-term memory
BP: Small GTPase-mediated signal transduction
KEGG: MAPK signaling pathway
BP: Negative regulation of neuron apoptosis
BP: Exocytosis
BP: Chromatin organization
BP: Protein transport
BP: Protein phosphorylation
MF: Oxidoreductase activity
Gene count
-log10(p)
Fold enrichment
B
WT + veh
3xTg + veh
Lamc2
Tnnc1
Gfap
Parp12
C1qa
Ighm
Syn1
Arrb1
Cacng2
Gabra3
Aldh7a1
Rgcc
log2 expression (all spatial spots [per region for violon plots])
Max
Min
Cortex
Hippocampus
Thalamus
Hypothalamus
C
Cortex
Hipp.
Thalamus
Hypoth.
Clusters
Genotype effect
SCDi in 3xTg
Log2(FC)
D
WT + veh
WT + SCDi
3xTg + veh
3xTg + SCDi
Hddc3
Fam81a
Pdyn
log2 expression (all spatial spots)

Electrocorticographic, Astrocytic and Transcriptomic Signatures in the Triple Transgenic Mouse Model of Alzheimer's Disease submitted to Stearoyl-CoA Desaturase Inhibition

Audrey Hector,[a-c] Tanya Leduc,[b,c,d,+] Maria João da Costa Caiado,[b,e,+]
Benoît Delignat-Lavaud,[b] Julien Dufort-Gervais,[c] Caroline Daneault,[f] Christine Des Rosiers,[f,g]
Clément Bourguignon,[b] Jean-Marc Lina,[c,h]
Karl Fernandes,[i] Jonathan Brouillette,[a,c] Valérie Mongrain[b,c,d,*]

[a]Department of Pharmacology and Physiology, Faculty of Medicine, Université de Montréal, C.P. 6128, Succ. Centre-Ville, Montreal, QC, H3C 3J7, Canada
[b]Centre de recherche du Centre hospitalier de l'Université de Montréal (CRCHUM), 900 rue St-Denis, Montreal, QC, H2X 0A9, Canada
[c]Center for Advanced Research in Sleep Medicine, Centre intégré universitaire en santé et services sociaux du Nord-de-l'Île-de-Montréal (CIUSSS-NIM), 5400 Gouin West blvd., Montreal, QC, H4J 1C5, Canada
[d]Departement of Neuroscience, Faculty of Medicine, Université de Montréal, C.P. 6128, Succ. Centre-Ville, Montreal, QC, H3C 3J7, Canada
[e]Groningen Institute for Evolutionary Life Sciences, University of Groningen, PO Box 72, 9700 AB Groningen, The Netherlands
[f]Metabolomic platform, Montreal Heart Institute Research Center, 500 Bélanger Street, Montréal, QC, H1T 1C8, Canada
[g]Department of Nutrition, Université de Montréal, Montreal, QC, H3C 3J7, Canada
[h]Département de génie électrique, École de Technologie Supérieure, 1120 Notre-Dame St West, Montreal, QC, H3C 0J8, Canada
[i]Faculty of Medicine and of Health Science, Université de Sherbrooke, 3001, 12e avenue Nord, Sherbrooke, QC, J1H 5N4, Canada

[+]These authors contributed equally to the work.
[*]Corresponding author: valerie.mongrain@umontreal.ca; CRCHUM, 900 rue St-Denis, Montreal, QC, H2X 0A9, Canada

Revised manuscript submitted for publication in: *Neuropharmacology*
Number of figures: 7
Number of supplementary figures: 11
Number of supplementary tables: 10

HIGHLIGHTS

- 3xTG-AD female mice sleep more specifically during the dark period.
- 3xTG-AD mice show altered electrocorticographic activity during wake/sleep states.
- Wake/sleep changes are not mitigated by a lipid metabolism-related treatment.
- Lipid droplets and astrocyte alterations in hippocampal CA1 are rescued by this treatment.
- Spatial transcriptomics reveal gene expression rescues in different brain regions.

Electrocorticographic, Astrocytic and Transcriptomic Signatures in the Triple Transgenic Mouse Model of Alzheimer's Disease submitted to Stearoyl-CoA Desaturase Inhibition

Audrey Hector,[a-c] Tanya Leduc,[b,c,d,+] Maria João da Costa Caiado,[b,e,+]
Benoît Delignat-Lavaud,[b] Julien Dufort-Gervais,[c] Caroline Daneault,[f] Christine Des Rosiers,[f,g]
Clément Bourguignon,[b] Jean-Marc Lina,[c,h]
Karl Fernandes,[i] Jonathan Brouillette,[a,c] Valérie Mongrain[b,c,d,*]

[a]Department of Pharmacology and Physiology, Faculty of Medicine, Université de Montréal, C.P. 6128, Succ. Centre-Ville, Montreal, QC, H3C 3J7, Canada
[b]Centre de recherche du Centre hospitalier de l'Université de Montréal (CRCHUM), 900 rue St-Denis, Montreal, QC, H2X 0A9, Canada
[c]Center for Advanced Research in Sleep Medicine, Centre intégré universitaire en santé et services sociaux du Nord-de-l'Île-de-Montréal (CIUSSS-NIM), 5400 Gouin West blvd., Montreal, QC, H4J 1C5, Canada
[d]Departement of Neuroscience, Faculty of Medicine, Université de Montréal, C.P. 6128, Succ. Centre-Ville, Montreal, QC, H3C 3J7, Canada
[e]Groningen Institute for Evolutionary Life Sciences, University of Groningen, PO Box 72, 9700 AB Groningen, The Netherlands
[f]Metabolomic platform, Montreal Heart Institute Research Center, 500 Bélanger Street, Montréal, QC, H1T 1C8, Canada
[g]Department of Nutrition, Université de Montréal, Montreal, QC, H3C 3J7, Canada
[h]Département de génie électrique, École de Technologie Supérieure, 1120 Notre-Dame St West, Montreal, QC, H3C 0J8, Canada
[i]Faculty of Medicine and of Health Science, Université de Sherbrooke, 3001, 12e avenue Nord, Sherbrooke, QC, J1H 5N4, Canada

[+]These authors contributed equally to the work.
[*]Corresponding author: valerie.mongrain@umontreal.ca; CRCHUM, 900 rue St-Denis, Montreal, QC, H2X 0A9, Canada

Revised manuscript submitted for publication in: *Neuropharmacology*
Number of figures: 7
Number of supplementary figures: 11
Number of supplementary tables: 10

DECLARATIONS

Authors' contributions

A.H., K.F., J.B., and V.M. designed the experiments and analytic plan. A.H. and J.D.-G. performed the animal experiments. A.H. and T.L. analyzed the electrophysiological and transcriptomic data. A.H. and M.J.d.C.C. conducted IHC experiments and analyses. B.D.-L. provided assistance with IHC and spatial transcriptomics, and conducted LD measurements. A.H., T.L., M.J.d.C.C. and V.M. performed statistical analyses and graphical representations. C.B. and J.-M.L. produced the code for scale-free activity analysis. C.D. and C.D.R. conducted fatty acid quantification and interpretation. A.H., T.L., M.J.d.C.C., and V.M. wrote and revised the manuscript. V.M. supervised all experiments and analyses. A.H., M.J.d.C.C., T.L., K.F., J.B., and V.M. provided funding. All authors approved the final version of the manuscript.

Conflict of interest

The authors have no conflict of interest to declare.

Data availability

Transcriptomic data are available at the GEO repository under accession number GSE275131. All other data are included in this article and its supplementary file. Raw data are available from the corresponding author upon reasonable request.

Acknowledgements

The authors are thankful to Laura Hamilton, Lewis Rhys Depaauw-Holt and Ciaran Murphy-Royal for help and advice related to experiment and interpretation. The authors also want to thank Aurélie Cleret-Buhot from the cellular imaging platform of the Centre de recherche du Centre hospitalier de l'Université de Montréal (CRCHUM) for precious help with the development of the microscopy pipeline, Véronique Barrès and Liliane Meunier from the molecular pathology platform (CRCHUM) for help with acquisition of histology images related to spatial transcriptomics, and Marie-Claude Therrien from the animal facility (CRCHUM) for assistance with animal transfer. Finally, the authors thank the staff from the Centre d’expertise et de services of Génome Québec (in particular Geneviève DonPierre) for sharing their expertise in RNA sequencing.

Funding

The research has been funded by a grant from the Canadian Institutes of Health Research to J.B. and V.M. (#437413), the Canada Research Chair in Sleep Molecular Physiology (V.M.), a scholarship from the Fonds de recherche du Québec - Santé (A.H.; #304560), a scholarship from the Natural Sciences and Engineering Research Council of Canada (T.L.; #569233-2022), and scholarships from the University of Groningen (M.J.d.C.C.).

Declaration of interests

☒ The authors declare that they have no known competing financial interests or personal relationships that could have appeared to influence the work reported in this paper.

☐The authors declare the following financial interests/personal relationships which may be considered as potential competing interests: